The Astrophysical Journal, 970:50 (22pp), 2024 July 20 https://doi.org/10.3847/1538-4357/ad4c6c

The Web Epoch of Reionization Lyα Survey (WERLS). I. MOSFIRE Spectroscopy of $z \sim$ 7–8 Lyα Emitters*

Olivia R. Cooper[1,23], Caitlin M. Casey[1,2], Hollis B. Akins[1], Jake Magee[1], Alfonso Melendez[1], Mia Fong[1], Stephanie M. Urbano Stawinski[3], Jeyhan S. Kartaltepe[4], Steven L. Finkelstein[1], Rebecca L. Larson[4], Intae Jung[5], Ash Bista[4], Jaclyn B. Champagne[6], Óscar A. Chávez Ortiz[1], Sadie Coffin[4], M. C. Cooper[7], Nicole Drakos[8], Andreas L. Faisst[9], Maximilien Franco[1], Seiji Fujimoto[1,24], Steven Gillman[2,10], Ghassem Gozaliasl[11], Santosh Harish[4], Taylor A. Hutchison[12,25], Anton M. Koekemoer[13], Vasily Kokorev[14], Jitrapon Lertprasertpong[4], Daizhong Liu[15], Arianna S. Long[1,24], Casey Papovich[16,17], R. Michael Rich[18], Brant E. Robertson[8], Margherita Talia[19,20], Brittany N. Vanderhoof[4,13], John R. Weaver[21], Katherine E. Whitaker[2,21], and Jorge A. Zavala[22]
[1] The University of Texas at Austin, 2515 Speedway Boulevard Stop C1400, Austin, TX 78712, USA
[2] Cosmic Dawn Center (DAWN), Denmark
[3] Department of Physics and Astronomy, University of California, Irvine, 4129 Frederick Reines Hall, Irvine, CA 92697, USA
[4] Laboratory for Multiwavelength Astrophysics, School of Physics and Astronomy, Rochester Institute of Technology, 84 Lomb Memorial Drive, Rochester, NY 14623, USA
[5] Space Telescope Science Institute, 3700 San Martin Drive Baltimore, MD 21218, USA
[6] Steward Observatory, University of Arizona, 933 N. Cherry Avenue, Tucson, AZ 85721, USA
[7] Department of Physics & Astronomy, University of California, Irvine, 4129 Reines Hall, Irvine, CA 92697, USA
[8] Department of Astronomy and Astrophysics, University of California, Santa Cruz, 1156 High Street, Santa Cruz, CA 95064, USA
[9] Caltech/IPAC, 1200 E. California Boulevard, Pasadena, CA 91125, USA
[10] DTU-Space, Technical University of Denmark, Elektrovej 327, DK-2800 Kgs. Lyngby, Denmark
[11] Department of Physics, University of Helsinki, P.O. Box 64, FI-00014 Helsinki, Finland
[12] Astrophysics Science Division, NASA Goddard Space Flight Center, 8800 Greenbelt Road, Greenbelt, MD 20771, USA
[13] Space Telescope Science Institute, 3700 San Martin Drive, Baltimore, MD 21218, USA
[14] Kapteyn Astronomical Institute, University of Groningen, P.O. Box 800, 9700 AV Groningen, The Netherlands
[15] Max-Planck-Institut für Extraterrestrische Physik (MPE), Giessenbachstraße 1, D-85748 Garching, Germany
[16] Department of Physics and Astronomy, Texas A&M University, College Station, TX 77843-4242, USA
[17] George P. and Cynthia Woods Mitchell Institute for Fundamental Physics and Astronomy, Texas A&M University, College Station, TX 77843-4242, USA
[18] Department of Physics and Astronomy, UCLA, PAB 430 Portola Plaza, Box 951547, Los Angeles, CA 90095, USA
[19] University of Bologna–Department of Physics and Astronomy "Augusto Righi" (DIFA), Via Gobetti 93/2, I-40129 Bologna, Italy
[20] INAF, Osservatorio di Astrofisica e Scienza dello Spazio, Via Gobetti 93/3, I-40129, Bologna, Italy
[21] Department of Astronomy, University of Massachusetts Amherst, 710 N Pleasant Street, Amherst, MA 01003, USA
[22] National Astronomical Observatory of Japan, 2-21-1 Osawa, Mitaka, Tokyo 181-8588, Japan
Received 2023 September 13; revised 2024 May 7; accepted 2024 May 14; published 2024 July 16

Abstract

We present the first results from the Web Epoch of Reionization Lyα Survey (WERLS), a spectroscopic survey of Lyα emission using Keck I/MOSFIRE and LRIS. WERLS targets bright ($J < 26$) galaxy candidates with photometric redshifts of $5.5 \lesssim z \lesssim 8$ selected from pre-JWST imaging embedded in the Epoch of Reionization (EoR) within three JWST deep fields: CEERS, PRIMER, and COSMOS-Web. Here, we report 11 $z \sim 7$–8 Lyα emitters (LAEs; three secure and eight tentative candidates) detected in the first five nights of WERLS MOSFIRE data. We estimate our observed LAE yield is ∼13%, which is broadly consistent with expectations assuming some loss from redshift uncertainty, contamination from sky OH lines, and that the Universe is approximately half-ionized at this epoch, whereby observable Lyα emission is unlikely for galaxies embedded in a neutral intergalactic medium. Our targets are selected to be UV-bright, and span a range of absolute UV magnitudes with $-23.1 < M_{\rm UV} < -19.8$. With two LAEs detected at $z = 7.68$, we also consider the possibility of an ionized bubble at this redshift. Future synergistic Keck+JWST efforts will provide a powerful tool for pinpointing beacons of reionization and mapping the large-scale distribution of mass relative to the ionization state of the Universe.

Unified Astronomy Thesaurus concepts: Lyman-alpha galaxies (978); Reionization (1383); Galaxy evolution (594)

machine-readable tables

1. Introduction

The first billion years of the Universe hosts its most pivotal transition—from a neutral to ionized medium—for which we have yet to determine primary drivers or a precise timeline. From the earliest work on this phase change (e.g., Arons & McCray 1970) to today, considerable progress has been made to constrain the processes and timing of this transition—the Epoch of Reionization (EoR)—through both theoretical and observational efforts. Observations of some of the first light sources as they ionized a then neutral intergalactic medium

* The data presented herein were obtained at the W. M. Keck Observatory, which is operated as a scientific partnership among the California Institute of Technology, the University of California and the National Aeronautics and Space Administration. The Observatory was made possible by the generous financial support of the W. M. Keck Foundation.
[23] NSF Graduate Research Fellow.
[24] NASA Hubble Fellow.
[25] NASA Postdoctoral Fellow.

(IGM) have revealed that the reionization process most likely finished around $z \sim 5.5$–6 (Zheng et al. 2011; Castellano et al. 2016; Kakiichi et al. 2016; Bosman et al. 2022) and was halfway completed by $z \sim 7$–8 (Robertson et al. 2013; Faisst et al. 2014; Finkelstein 2016). Around this halfway point, a high neutral fraction of the IGM has been fairly constrained from somewhat sparse measurements of Lyα emitters (LAEs), where the conversion to a neutral fraction has a high systematic uncertainty (Treu et al. 2013; Hoag et al. 2019; Mason et al. 2019; Bolan et al. 2022).

While observations have provided some constraints on the timeline of the EoR, the duration and patchiness of reionization, as well as its main driving sources, remain unclear. In the case where all galaxies have relatively high escape fractions of ionizing photons ($f_{\rm esc} \sim 20\%$)—therefore, massive, UV-bright galaxies dominate reionization (Naidu et al. 2020)—a late-reionization is favored. However, some observations show that galaxies with high $f_{\rm esc}$ are rare (Izotov et al. 2016), with small samples of local detections of cosmologically relevant escape fractions $f_{\rm esc} > 5\%$ (e.g., Flury et al. 2022) and few observations with very high escape fractions $f_{\rm esc} \gtrsim 20\%$ (e.g., Izotov et al. 2018; Saha et al. 2020; Marques-Chaves et al. 2021; Saxena et al. 2023a). Simulations predict that $f_{\rm esc}$ depends on halo mass, with higher $f_{\rm esc}$ from fainter galaxies in lower-mass halos (Paardekooper et al. 2015; Faisst 2016; Bremer & Dayal 2023). This suggests the case where more numerous UV-faint galaxies dominate reionization, and favors an earlier start to reionization that evolves smoothly in time (Mason et al. 2015; Finkelstein et al. 2019). Around the instantaneous redshift of reionization ($z_{\rm reion} = 7.68 \pm 0.79$; Planck Collaboration 2020)—which serves as a mean reionization redshift by assuming the process was instantaneous—the former scenario predicts the IGM is $<1/3$ ionized, while the latter scenario (wherein faint galaxies dominate) predicts $>1/2$ of the IGM is ionized (Finkelstein et al. 2019). Taking a census of massive galaxies at $z > 7$ can help answer both questions regarding the duration and sources of reionization; in particular, did intrinsically bright galaxies or faint galaxies drive reionization?

In constraining this problem, we are faced with a relative shortage of intrinsically UV-bright $z > 7$ galaxies currently known and spectroscopically confirmed (see Ouchi et al. 2020, for a summary of the 15 $z > 7.2$ spectroscopic confirmations pre-JWST). The pre-JWST sample of $z > 7$ EoR galaxies has been gathered and confirmed via direct detection of candidate Lyα Break Galaxies (LBGs) in relatively small, pencil-beam fields with Hubble Space Telescope (e.g., Bunker et al. 2010; Finkelstein et al. 2010, 2012; McLure et al. 2010; Oesch et al. 2012; Yan et al. 2012), from sources with "IRAC excess" attributed to intense [O III]+Hβ line emission at $z \sim 8$ polluting the IRAC 4.5 μm band (e.g., Smit et al. 2015; Roberts-Borsani et al. 2023), and from spectroscopic follow-up mainly targeting Lyα (e.g., Ono et al. 2012; Shibuya et al. 2012; Finkelstein et al. 2013; Oesch et al. 2015; Zitrin et al. 2015; Inoue et al. 2016; Song et al. 2016; Hoag et al. 2017; Stark et al. 2017; Hu et al. 2019; Jung et al. 2019, 2020; Harish et al. 2022; Larson et al. 2022; Wold et al. 2022) or [C II] emission lines (e.g., Smit et al. 2018; Bouwens et al. 2022; Schouws et al. 2022). Now with JWST, perhaps the most impressive early results illustrate its ease of spectroscopic detection for galaxies that were previously undetectable because spectra have been gathered for relatively large samples of EoR galaxies from both NIRSpec (e.g., Arrabal Haro et al. 2023; Bunker et al. 2023; Cameron et al. 2023; Curtis-Lake et al. 2023; Fujimoto et al. 2023) and the NIRCam Grism (e.g., Oesch et al. 2023).

Several of these spectroscopically confirmed early EoR galaxies (both from JWST and pre-JWST) exhibit Lyα in emission (e.g., Oesch et al. 2015; Zitrin et al. 2015; Hashimoto et al. 2018; Hoag et al. 2018; Pentericci et al. 2018; Tang et al. 2023; Jones et al. 2024; Nakane et al. 2024; Saxena et al. 2024), with detections of Lyα as high as $z_{\rm spec} = 10.60$ (GN-z11; Bunker et al. 2023). However, detecting Lyα from galaxies embedded in the EoR—especially at $z > 8$ when the Universe is thought to have been predominantly neutral—involves both technical and physical challenges. From a technical standpoint, while redshift identification via rest-frame optical nebular emission lines is very efficient with NIRSpec, Lyα can still be elusive, even to JWST. For example, while Lyα was detected in GN-z11 at $z_{\rm spec} = 10.60$ (anchored by multiline confirmation in Bunker et al. 2023), it was only seen in higher resolution spectra and was undetected in PRISM observations. Additionally, Lyα detections with NIRSpec can be difficult due to slit losses, particularly important for Lyα emission which can extend beyond the small 0.″3 NIRSpec slitlets. As demonstrated for the $z = 5.66$ LAE in Jiang et al. (2023), JWST/NIRSpec fails to detect Lyα emission that is robustly captured with ground-based spectroscopic instruments. While JWST is highly efficient for spectroscopic redshifts, ground-based spectra such as those we present here remain valuable for studies of Lyα in the EoR. Detecting Lyα is also challenging from a physical perspective because Lyα photons from EoR galaxies should resonantly scatter by the mostly neutral IGM at a relatively low threshold for H I column density ($N_{\rm HI} > 10^{17} {\rm cm}^{-2}$; Dijkstra et al. 2014; Stark 2016). This concern is partially alleviated by assuming an inhomogeneous reionization process.

Indeed, cosmological simulations indicate that reionization was likely a patchy process (Furlanetto et al. 2017; D'Aloisio et al. 2018), producing ionized bubbles in the surrounding IGM growing from 5 to 20 cMpc at $z > 8$ to 30–100 cMpc at $z \sim 7$ (10′–40′). Constraints from spectra of quasars near the end of reionization support this picture of patchiness (e.g., Becker et al. 2015). Observational clues of this patchy reionization have also been noted in the distribution of LAEs within the EoR and the large-scale bubbles of ionization they may live in. Recent studies report two or more spectroscopically confirmed sources at the same redshift (e.g., Jung et al. 2019; Tilvi et al. 2020), from which a bubble size is inferred based on estimated ionizing radiation encompassing galaxies within that overdensity. For example, Larson et al. (2022) find a candidate LAE at $z = 8.7$ with Keck/Multiobject Spectrometer for Infrared Exploration (MOSFIRE) near a known source at a similar redshift (Zitrin et al. 2015) in the Extended Groth Strip (EGS), and report the tentative, serendipitous result of an ionized bubble. Further analysis of fainter galaxies within the $z = 8.7$ overdensity in EGS suggest this ionized bubble could be fairly large (Tang et al. 2023; Whitler et al. 2024, R. Larson et al., 2024, in preparation). Other studies report apparent overdensities in the EoR—potentially pointing to large ionized bubbles—but are limited to uncertain photo-z's to approximate an encompassed comoving volume (e.g., Endsley et al. 2021; Hu et al. 2021). Results from JWST spectroscopy support this connection between overdensities and ionized bubbles in the EoR; Witstok et al. (2024) find an enhancement LAEs within overdensities, and note the utility of LAEs as tracers of ionized

bubbles. These sparse observations loosely match theoretical expectations, with the tentative $z = 6.8$ bubble (Endsley et al. 2021) at an estimated radius of ∼23 cMpc, and the potential $z = 8.7$ overdensity up to ∼30 cMpc (Larson et al. 2022; Whitler et al. 2024). Recent simulations show that for a fixed ionization fraction, bubble size distributions vary with the dominant source of ionizing output, wherein the dominance of low-mass halos produces a lot of smaller bubbles and the dominance of high mass halos produces fewer but larger bubbles (Kannan et al. 2022). The ionization history is also encoded in the patchiness of reionization; at $z \sim 7.5$–8, ionized bubbles should be rare in the late-reionization scenario and more common in the early-reionization scenario (e.g., Finkelstein et al. 2019).

The Web Epoch of Reionization Lyα Survey (WERLS)[26] is designed to conduct this census of Lyα emission in a sample of photometrically selected UV-bright ($M_{\rm UV} \lesssim -20$) EoR galaxies in areas covered by JWST imaging, on scales large enough to capture bubbles. WERLS is designed to expand the sample of spectroscopically confirmed EoR LAEs at $z \sim 5.5$–8, as well as map ionized bubbles in the IGM on large scales. In this paper, we present the first semester of Keck I/MOSFIRE data from WERLS, including spectra for a subset of UV-bright EoR LAEs from $z \sim 7$–8. We describe the sample and observations in Section 2, and in Section 3 we present analysis of the spectroscopic data. In Section 4, we detail photometric and spectroscopic characterization of the individual sources, in Section 5 we discuss the implications of our measurements, and we present a summary in Section 6. The full target list, including spectroscopic results and redshift measurements for filler targets, is presented in the appendix. All magnitudes are quoted in the AB system (Oke & Gunn 1983), we assume a Chabrier initial mass function (Chabrier 2003), and we assume a Planck cosmology throughout this paper, adopting $H_0 = 67.74\,{\rm km\,s^{-1}\,Mpc^{-1}}$ and $\Omega_\lambda = 0.691$ (Planck Collaboration 2016).

2. Observations and Sample

WERLS is a 29-night NASA key strategic mission support program (PIs: Casey & Kartaltepe) using two multiobject spectrometers on Keck I, MOSFIRE (McLean et al. 2012), and the Low Resolution Imaging Spectrometer (LRIS; Oke et al. 1995; Rockosi et al. 2010). The primary objective of WERLS is to target ∼800 galaxy candidates embedded within the latter half of the EoR in order to conduct a census of Lyα and correlate the Lyα-inferred location of ionized structures in the IGM to galaxy density maps measured with JWST/NIRCam.

By combining these Lyα detections with JWST imaging (currently being obtained), we can then map the underlying galaxy density distribution in the same areas where we have mapped the inferred ionization state of the IGM. The WERLS program uses two instruments: LRIS, optimal for detecting Lyα at $z \lesssim 7$, and MOSFIRE in *Y*-band, optimal for detecting Lyα at $z \sim 7$–8.

In this paper, we focus only on candidate $z \sim 7$–8 LAEs detected using MOSFIRE data collected over the first five nights of WERLS in the 2022A semester. Initial results from LRIS observations in 2022A will be presented in a companion paper (S. Urbano Stawinski et al. 2024, in preparation).

2.1. Sample Selection

Our spectroscopic targets have been selected specifically across three extragalactic fields that have approved deep near-infrared imaging from JWST/NIRCam during its first year of observations: the COSMOS-Web Cycle 1 program (0.54 deg^2, GO#1727, PIs: Casey & Kartaltepe, Casey et al. 2023), the Cosmic Evolution Early Release Science Survey (CEERS, 0.03 deg^2, ERS#1345, PI: S. Finkelstein, Finkelstein et al. 2022, 2023),[27] and the Public Release IMaging for Extragalactic Research Cycle 1 program (PRIMER, 0.07 deg^2, GO#1837, PI: J. Dunlop, Dunlop et al. 2021) in the Cosmic Assembly Near-infrared Deep Extragalactic Legacy Survey (CANDELS; Faber 2011) regions of the COSMOS and Ultra Deep Survey (UDS) fields. These fields together encompass 0.7 deg^2 and constitute the largest (by area) extragalactic surveys planned in the first year of JWST observations. Here, we describe the target selection used for the MOSFIRE observations in each of the three fields.

Within the COSMOS-Web footprint, we first select WERLS targets via deep ground-based imaging from the COSMOS2020 catalog (Weaver et al. 2022). These COSMOS targets include EoR candidates selected via well-constrained photometric redshifts from analysis of all Spitzer data (Euclid Collaboration et al. 2022) in addition to deep near-infrared and optical imaging from UltraVISTA DR4 (McCracken et al. 2012) and Subaru/Hyper Suprime-Cam, which increases depth by ∼1 mag relative to previous observations in the same field (Laigle et al. 2016). We perform photometric selection using the `Farmer` photometry (Weaver et al. 2019) and use photometric redshifts fit using LEPHARE (Arnouts et al. 1999; Ilbert et al. 2006; Arnouts & Ilbert 2011). The total WERLS sample (selected for both LRIS and MOSFIRE) has been selected within the COSMOS-Web footprint as $J < 26$ continuum sources with $z_{\rm phot} > 6$ with ⩾95% of their redshift probability density distribution (PDF) above $z = 5.5$, a conservative lower-redshift bound to the end of reionization (Becker et al. 2015). WERLS targets are selected to be UV-bright; 90% of the sample have $M_{\rm UV} \lesssim -20$ if confirmed at their photometric redshifts, this is roughly equal to the characteristic magnitude M_* of the luminosity function at these redshifts (Finkelstein et al. 2019).

Additional targets within COSMOS, as well as target selection in the EGS and UDS fields, have been selected from deep Hubble Space Telescope (HST) and Spitzer imaging from the CANDELS fields (Grogin et al. 2011; Koekemoer et al. 2011; Ashby et al. 2015) with $J < 26$ and with the same redshift criteria of $z_{\rm phot} > 6$ with 95% of their redshift PDF above $z = 5.5$. This photometric selection for CANDELS sources utilizes SOURCEEXTRACTOR photometry (Bertin & Arnouts 1996) and EAZY redshift PDFs (Brammer et al. 2008). Given the increased depth of CANDELS near-infrared observations compared to ground-based observations, we also include slightly fainter EoR candidates ($J < 27.5$) but include them as fillers rather than primary targets. In these CANDELS regions, we used the photometric catalogs and photometric

[26] This survey was originally named *Webb* Epoch of Reionization Lyα Survey, in reference to the telescope's name, but was later renamed to emphasize the scientific goal of mapping the cosmic web on large scales, as well as to be inclusive and supportive to members of the LGBTQIA+ community.

[27] Available for download at ceers.github.io/releases.html and on MAST as High Level Science Products via doi:10.17909/z7p0-8481 (Finkelstein et al. 2023).

redshift results from Finkelstein et al. (2022). We selected $z > 6$ galaxies using a modified version of the Finkelstein et al. (2022) selection criteria (which had been optimized for $z > 8.5$), requiring $z\_best > 6$, and 95% of the redshift PDF above $z = 5.5$.

Lower-redshift filler targets were included in the sample to increase the efficiency of observations, selected by magnitude and photometric redshift from the COSMOS2020 and CANDELS photometric catalogs. We select three categories of filler targets based on different redshift ranges optimized for other prominent emission lines: Hα -emitters at $0.5 < z < 0.7$, [O II]-emitters at $1.6 < z < 2.0$, and C III]-emitters at $4.1 < z < 4.9$. Spectroscopic information for the 166 filler targets (an average of ∼18 fillers per slit mask, just over half of the targets per mask) are presented in the appendix, along with any new spectroscopic redshift measurements. Stars (used for alignment and for flux calibration) were also placed on each mask; these are taken from Gaia DR3 (Gaia Collaboration et al. 2023) and registered to the same reference astrometry as our source catalogs.

The broader WERLS Primary target sample (Lyα targets selected photometrically at $z_{\rm phot} \gtrsim 5.5$) is optimized for observability with both LRIS and MOSFIRE; targets are then sorted into subsamples based on their redshift PDFs:

1. Primary MOSFIRE targets: $\gtrsim$50% of their photometric redshift PDF within $7.0 < z < 8.2$, corresponding to the MOSFIRE *Y*-band wavelength coverage for Lyα emission.
2. Primary LRIS targets: $\gtrsim$50% of their photometric redshift PDF at $z < 7$, corresponding to the LRIS wavelength coverage for Lyα emission.
3. Primary targets for both MOSFIRE+LRIS: broader redshift PDFs split roughly evenly between the wavelength ranges of both instruments, with ∼25% of their photometric redshift PDFs within $7.0 < z < 8.2$.

The total WERLS selection collates a sample of EoR targets selected from recently published extragalactic catalogs, namely from a reprocessing of CANDELS data to create an EoR-optimized sample (Finkelstein et al. 2022) and from COSMOS2020 (Weaver et al. 2022). From these catalogs, we additionally visually vet the objects to remove imaging artifacts such as hot pixels or features in the extended PSF of bright stars. COSMOS2020 sources span the 0.54 deg^2 of the COSMOS-Web footprint and make up 65% of the primary target sample. CANDELS covers ∼0.15 deg^2 in three fields and contributes 35% of the primary target sample, as well as fainter filler targets down to ∼28 mag. This results in a total of 2034 primary targets, or 1.32 per square arcmin in the total CANDELS footprints and 0.68 per square arcmin in the wider COSMOS footprint. The distribution of photometric redshifts and *J*-band magnitudes for the full WERLS sample is shown in Figure 1.

From this COSMOS2020 and CANDELS-based target list, we then designed optimized slit mask configurations in the MOSFIRE Automatic GUI-based Mask Application (MAGMA[28]) for our Keck/MOSFIRE observations. The fields and targets observed relative to the JWST deep fields in which they lie are shown in Figure 2. Mask pointings were selected to maximize the number of EoR targets on slits, and, in general,

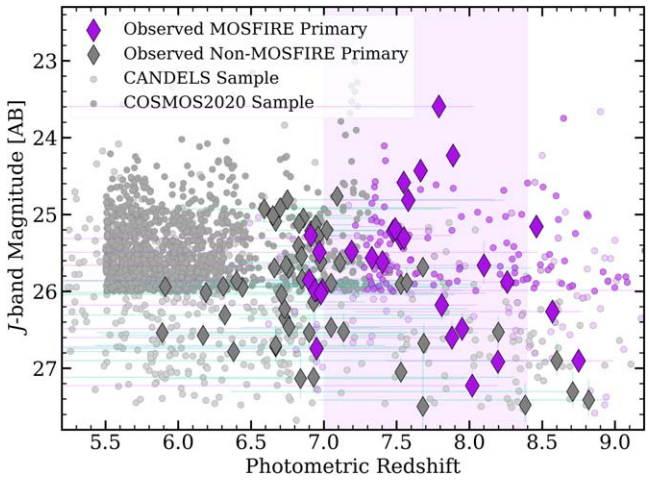

Figure 1. *J*-band magnitude (AB) vs. photometric redshift for the full WERLS sample. Diamonds denote the subsample that was placed on slits, and therefore were observed with MOSFIRE; circles show the remaining WERLS targets that were not observed in 2022A, wherein darker gray circles are selected from COSMOS2020 and lighter gray circles are CANDELS selected. All points colored purple are MOSFIRE Primary targets; gray points are NonMOSFIRE Primary targets, which includes both MOSFIRE+LRIS Primary targets, and LRIS Primary targets. The range of redshifted Lyα emission accessible with MOSFIRE *Y*-band is represented via light purple region.

targets were prioritized by brightness ($J_{\rm mag}$ as measured in UltraVISTA *J*-band or HST WFC3/F125W, drawn from the survey from which a given source was selected) and photometric redshift corresponding to emission lines falling within the MOSFIRE *Y*-band wavelength coverage. Each mask also had at least one star (classified as unresolved using HST imaging, and between 16 and 19 mag) placed on a slit to monitor seeing conditions and potential pointing drift throughout observations.

Target selection for 2022A MOSFIRE masks across the aforementioned three categories resulted in 114 WERLS Primary Lyα targets for our nine 2022A MOSFIRE pointings. From these 114 WERLS Primary targets, 33 were MOSFIRE Primary targets, 54 were both MOSFIRE+LRIS Primary targets, and 27 were LRIS Primary targets. The subsample of observed targets are distinguished from the full WERLS sample in Figure 1. Given the breadth of the photometric redshift PDFs, we expect that some LRIS Primary targets might be detected in Lyα emission within the MOSFIRE wavelength range, and vice versa; so, lower-redshift EoR candidates are still added to MOSFIRE masks as high priority fillers, though they do not drive the choice of pointing, which was based on the higher-z MOSFIRE Primary subsample. Furthermore, depending on specific LRIS and MOSFIRE mask design, a subset of the WERLS Primary targets were observed with both instruments in order to capture a wider wavelength range for possible Lyα detection.

Primary target source density was highest within the CANDELS fields due to their depth, and as a result COSMOS pointings for 2022A were clustered in the PRIMER-COSMOS area. The effective area covered by the nine slit masks is ∼0.05 deg^2 across the three fields, with the majority of the covered area in COSMOS. In total, for the nine MOSFIRE masks observed in 2022A, 276 galaxy candidates (114 WERLS Primary and 162 fillers) and 15 stars were placed on slits. We compare the number of high priority targets that were placed on slits, and therefore were observed, to the total number of high

[28] https://www2.keck.hawaii.edu/inst/mosfire/magma.html

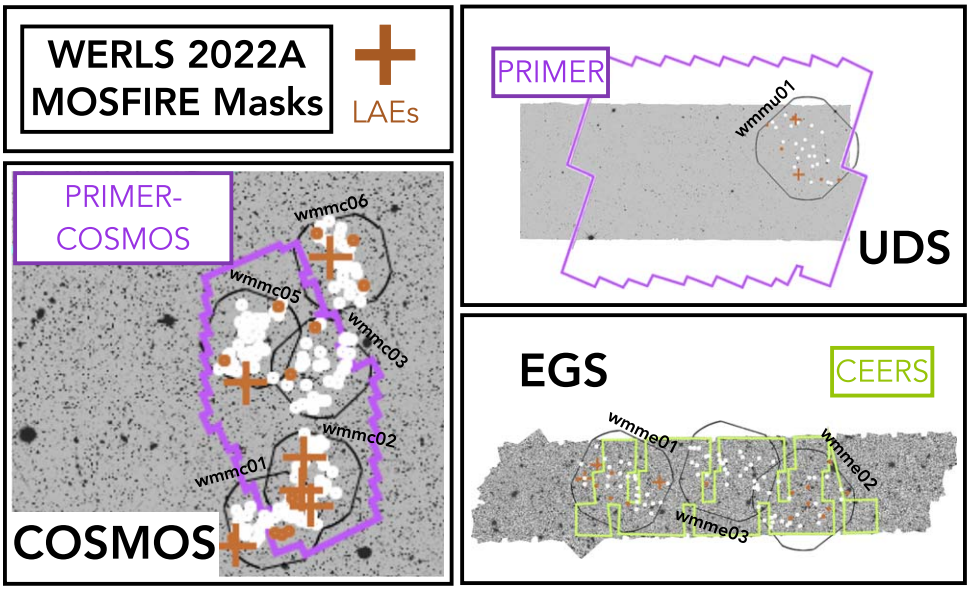

Figure 2. Positions of our WERLS 2022A MOSFIRE observations with the field of view of each MOSFIRE mask in black boxes (labeled by mask name) and all targets in each mask marked as white points. MOSFIRE Primary targets are noted as orange points, and the EoR LAEs reported in this paper are marked with orange pluses. In each field—COSMOS, UDS, and EGS—the JWST coverage is overlaid with PRIMER in purple and CEERS in chartreuse. COSMOS-Web coverage extends beyond the entire image of COSMOS shown here. The figures are projected on the CANDELS HST/F160W images for EGS and UDS, and the COSMOS2020 chimean image for COSMOS.

priority targets that fall within each mask area. Limiting to MOSFIRE Primary targets only, we observed 100% of targets within each mask area; this is expected because the MOSFIRE Primary targets drove pointing positions and were the highest priority targets. Expanding to NonMOSFIRE Primary targets (which included lower-redshift EoR targets), we find that approximately 60% of targets within each mask were observed (see Table 1 for the fraction observed for each mask). This is primarily due to both prioritizing MOSFIRE Primary targets on slits, and the high source density of NonMOSFIRE Primary targets.

2.2. Keck/MOSFIRE Observations

Observations were taken with MOSFIRE (McLean et al. 2012) on the Keck I telescope using the *Y*-band spectroscopic filter to optimize for detection of Lyα redshifted to $7.0 < z < 8.2$. Observations were obtained over five nights in 2022A: 2022 February 12, 2022 February 13, 2022 February 14, 2022 March 14, and 2022 April 17 UTC. Individual science frames were taken with 180 s exposures, with a goal of $\sim$4 hr of total exposure time per mask. We use a standard ABBA dither pattern with nod distance of 1.″25 (unless contaminants landed on high priority slits at this distance, then 1.″5 nods were taken). Exposures in *Y*-band were 180 s and taken in MCDS sampling mode with 16 reads; for each mask we aim for 20 ABBA sequences to achieve a nominal 4 hr total exposure time, but there are cases where we took more sequences if weather conditions were not ideal.

Four of the nine slit masks were not observed for the full 20 sequences, mostly due to limited observability due to weather; observational details for each MOSFIRE slit mask are listed in Table 1. We adopted slit widths of 0.″7 (affording a spectral resolution of $R\sim3500$) or 1.″0 depending on the seeing during observations. The seeing varies through the nights from 0.″6 to 1.″3, as measured directly from our spectroscopic data using the monitoring star. Weather conditions varied across the five nights: 2022-Feb-12 was clear with good seeing throughout the night; 2022 February 13 was clear with variable seeing throughout the night; 2022 February 14 had wind, fog, and snow, leading to the dome closing twice and poor seeing; 2022 March 14 was clear with good seeing; and 2022 April 17 began with high humidity and delays in the dome opening followed by some cloud cover the rest of the night, leading to moderate seeing.

2.3. MOSFIRE Spectroscopic Data Reduction

The data were reduced using two reduction pipelines independently to ensure robust noise characterization in order to build confidence in our candidate faint line detections for these high redshift targets.

First, we use the `PypeIt` data reduction package (Prochaska et al. 2020), which is designed to be a general use spectroscopic pipeline and can be used for a range of instruments and facilities. We iteratively worked with the `PypeIt` team to determine the optimal data reduction configuration for Keck I/MOSFIRE parameters in `PypeIt` and reduce the data in ABBA sequence blocks, using the spectral trace of a bright star in one of the slits on each mask as a position reference. The output from `PypeIt` is reduced and co-added 2D spectra, from which we optimally extract 1D spectra at the centroid of the emission line using the technique of Horne (1986), with a 7 pixel (1.″26) spatial aperture, matched to the typical seeing FWHM level from our observations. In a few cases, candidate emission line detections were slightly offset by 1–2 pixels from the target position; however, in all cases the candidate line was $<$0.″3 away from the source centroid, which is well within expectations given positional accuracy and possible Lyα emission offsets from the broadband imaging centroid. We also extract 1D spectra using a boxcar for comparison, but typically achieve a higher S/N using optimal extraction; we ultimately adopt the optimally extracted 1D spectra for our measurements.

Table 1
Summary of 2022A MOSFIRE Observations

Mask Name	R.A.	Decl.	Date(s) Observed[a] (UTC)	$N_{\rm targs}$[b]	$N_{\rm fillers}$[c]	$N_{\rm obs}/N_{\rm total}$[d]	$N_{\rm seq}$ (# ABBA)	Slit Width (arcsec)	Seeing[e] (arcsec)	Airmass	5σDepth[f] (mag)
wmmu01	02:17:04.68	–05:10:30.00	Feb 12, 13, 14	5 (23)	9	1.0 (0.5)	14	0.7–1.0	0.7–1.2	1.4	20.4
wmmc06	10:00:16.13	+02:29:18.60	Apr 17	2 (6)	19	1.0 (0.6)	15	1.0	0.9–1.3	1.0	20.0
wmmc03	10:00:22.34	+02:21:57.60	Feb 13, 14 & Mar 14	9 (13)	10	1.0 (0.7)	33	0.7–1.0	0.9–1.3	1.7	20.7
wmmc02	10:00:24.60	+02:14:19.68	Feb 12, 13	6 (13)	13	1.0 (0.6)	20	0.7–1.0	0.7–1.3	1.6	20.5
wmmc01	10:00:35.47	+02:11:31.92	Feb 12	4 (14)	13	1.0 (0.6)	20	0.7	0.6–0.9	1.6	21.4
wmmc05	10:00:41.57	+02:24:03.96	Feb 14 & Mar 14	3 (8)	18	1.0 (0.6)	32	0.7–1.0	0.7–1.3	1.1	21.3
wmme02	14:19:24.05	+52:48:20.88	Apr 17	1 (20)	11	1.0 (0.6)	17.5	1.0	0.8–1.3	1.2	19.9
wmme03	14:19:35.83	+52:53:24.36	Mar 14	1 (8)	25	1.0 (0.6)	8	0.7	0.6–0.9	1.2	20.0
wmme01	14:20:10.44	+52:58:28.92	Feb 12, 13, 14 & Mar 14	3 (12)	21	1.0 (0.7)	20	0.7–1.0	0.7–1.2	1.2	20.3

Notes.
[a] All dates listed are from the year 2022.
[b] Number of MOSFIRE Primary targets on mask (excludes filler targets); in parentheses we give the total number of WERLS EoR targets (some of which are fainter than the primary sample).
[c] Number of filler targets on mask.
[d] Fraction of MOSFIRE Primary targets observed out of the total MOSFIRE Primary targets within a given mask area; in parentheses we give the same fraction for the NonMOSFIRE Primary WERLS EoR targets.
[e] Seeing measured from the full-width half maximum (FWHM) estimated from continuum object (bright star) placed on each science mask.
[f] Limiting 5σmagnitude measured via *Y*-band magnitude and MOSFIRE signal-to-noise (S/N) of bright star placed on each science mask.

Second, we use the public MOSFIRE data reduction pipeline (MOSFIREDRP[29]) to reduce the raw data. The MOSFIREDRP pipeline provides a sky-subtracted, flat-fielded, and rectified 2D slit spectrum per slit object. The reduced spectra are wavelength-calibrated using telluric sky emission that is built specifically for the instrument. We extract 1D spectra from the combined 2D spectra via both optimal and boxcar extraction schemes as above, ultimately adopting the optimally extracted 1D spectra.

While some teams have reported that there is nonnegligible slit drift in the spatial direction (up to $\sim$1 pixel hr^{-1}) in their MOSFIRE observations that necessitated correction (e.g., Kriek et al. 2015; Song et al. 2016; Jung et al. 2019; Hutchison et al. 2020; Larson et al. 2022), we checked slit alignments carefully during the course of our observations using our reference star and found no significant slit drift. Note that all of our masks were only observed for a maximum of four hours where many data sets that see significant drift coadd data taken over a longer duration. While drift is automatically accounted for in our `PypeIt` reductions, it is not accounted for in our MOSFIREDRP reductions, except when co-adding data from different nights where it was critical to account for a global offset in the final reduced product.

To flux calibrate our spectra, we measure scaling factors based on stars placed on science slits on each mask. This allows our calibration to account for variations in observing conditions over the duration of observations taken for each mask. We match the known UltraVISTA *Y*-band magnitude (McCracken et al. 2012) to the observed magnitude in MOSFIRE *Y*-band measured from our spectra for each mask's star (accounting for throughput), converting between the two filters by using a flux factor measured from convolving each filter transmission profile with a model stellar spectrum of the same stellar type (Castelli & Kurucz 2003). We then compute and apply the wavelength-dependent scaling factor to the science spectra.

3. Spectroscopic Analysis

In this first WERLS paper, we focus only on the goal of taking a census of LAEs in the EoR, limited to the WERLS MOSFIRE 2022A data set in hand. Here, we present the MOSFIRE spectroscopic constraints for this initial sample.

3.1. Lyα Emission Line Vetting

Our candidate Lyα emission lines were all first identified via visual inspection of the 2D spectra, initially from either the MOSFIREDRP or `PypeIt` reduction. Inclusion in this paper as a tentative or secure detection requires the candidate emission line to be present at $\geqslant 4\sigma$ in both independent reductions, which reinforces our confidence in the robustness of the detection. To calculate the S/N, we take the total integrated signal from 1D spectrum directly, around a small region centered on the peak as measured via the Gaussian fit to the line. We estimate errors by bootstrapping from observed error over the same region of the 1D spectrum, excluding portions of the spectrum strongly affected by OH sky lines. We check for a bright positive signal with spatial width well-matched to seeing and spectral width at least as broad as one spectral resolution element. Such a positive signal then has an integrated S/N greater than the average noise (with a threshold of $\geqslant 4\sigma$, consistent with other Lyα spectroscopic works, e.g., Jung et al. 2022), with OH forest sky emission features masked out. We verify that candidate emission line detections also have negative signals; real astronomical signal should be accompanied by symmetric negative signals with S/N $\sqrt{2}$ lower than the positive signal, spatially offset above and below the positive signal at the expected separation based on the mask's adopted nod amplitude. Using these criteria, we inspect both data reduction products to ensure the feature is not an obvious artifact. All LAEs reported in this paper satisfied our criteria in both reductions; in some cases the S/N of the line varied slightly within the noise between reductions.

To ensure the nature of the emission line candidates as (spectrally isolated) Lyα, we search for multiple emission lines in the *Y*-band spectra, which implies the original line is not Lyα and the source is at a lower redshift. A likely contaminant in this case is a source with [OII]$\lambda\lambda$3727, 3729 emission; galaxies with [OII] emission in *Y*-band may be misidentified as EoR galaxies if the Balmer break is mistaken for the Lyα break in a photometric redshift solution. However, in this case, given the spectral resolution of our MOSFIRE data, this doublet should be resolvable (at 7 $-8\,\AA$ at the expected [OII]-emitter redshift of $z \sim 1.8$) and therefore distinguishable from Lyα for uncontaminated (with respect to sky lines) spectral regions broader than the doublet width. For all candidate lines, we also verify alignment on the slit mask by optimally extracting the 1D spectrum at the spatial position of the detection and verify the spatial positions of the negatives match expectations given the nod amplitude for those observations.

To further assess the credibility of the Lyα identification, we consider the available photometric constraints. Any excess emission in Spitzer/IRAC Channel 2 (4.5 μm) over Spitzer/IRAC Channel 1 (3.6 μm) provides increased credibility for our Lyα emission line candidates because the presence of strong [OIII]+Hβ emission would cause an "IRAC excess" from $z \sim 7-9$, encompassing our entire target redshift range. Additionally, by examining *HST*/UltraVISTA cutouts of the target showing the slit overlay, we check for potential low-z contaminants by ruling out any large, bright targets at or near the target position on the slit that could be serendipitous sources of emission lines.

3.2. LAEs

From this first round of emission line searching and vetting, we find 35 candidate EoR LAEs out of 114 primary targets, for which we compiled all available spectroscopic and photometric information. This compiled information was visually inspected and vetted by 22 of this paper's coauthors independently. Each of the 22 coauthors commented on the source and ranked its quality as "Bogus", "Very Tentative", "Tentative", or "Secure", which were then assigned numerical values 1–4. Note that detections were vetted not only by visual inspection but by a holistic review of the photometric redshift distribution, broadband photometry and spectral energy distribution (SED), MOSFIRE spectrum, and measured S/N of the emission line.

From this inspection, we settled on 11 total LAEs to present in this paper based on our aggregate confidence in their reliability. This sample of 11 was divided into two categories: secure ($N = 3$) and tentative ($N = 8$). We ultimately categorize sources using all available data with a holistic assessment, described as follows. Secure sources were strongly detected in both MOSFIREDRP and `PypeIt` reductions, have a clear Lyα break in their photometry,

[29] https://keck-datareductionpipelines.github.io/MosfireDRP/

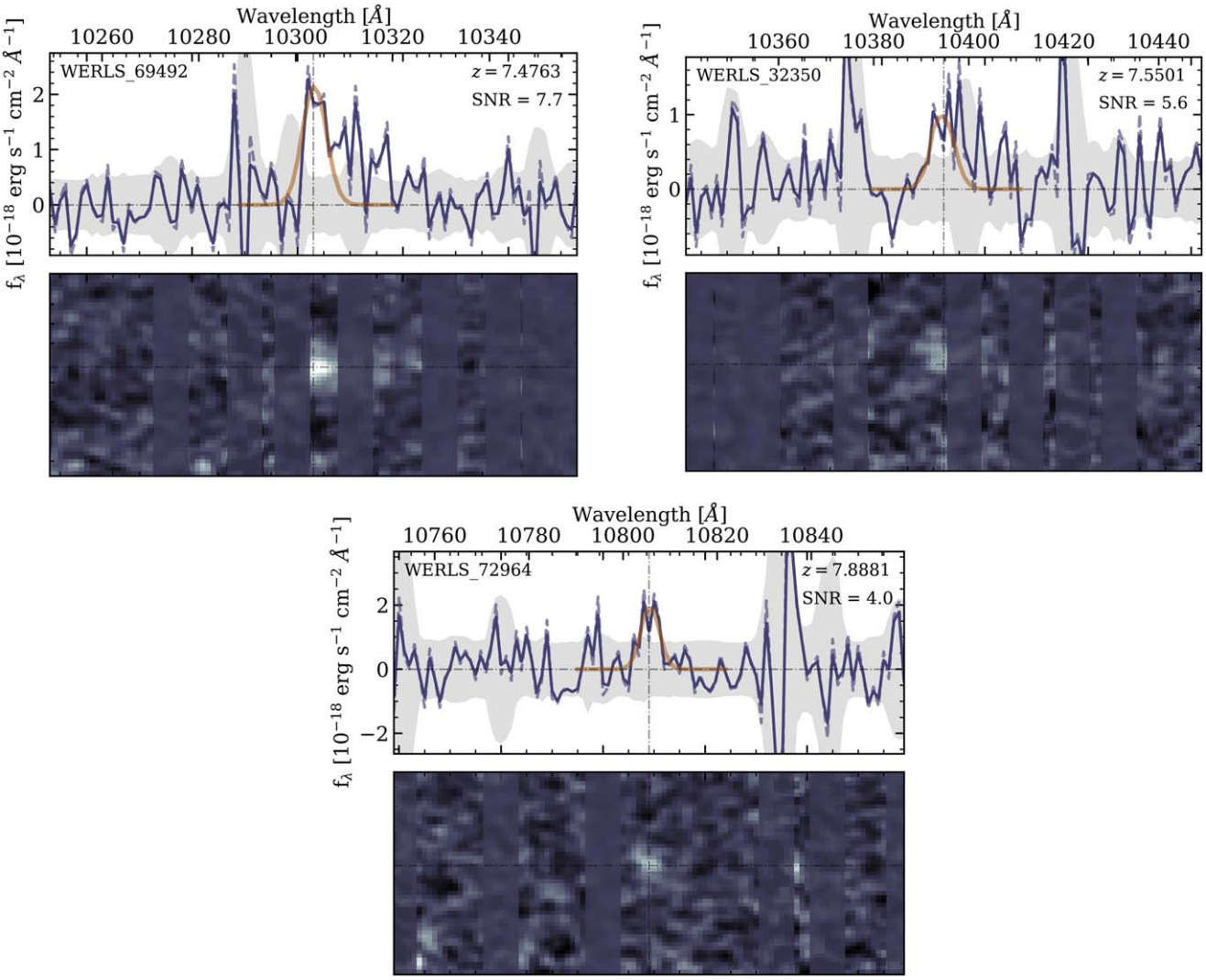

Figure 3. WERLS MOSFIRE *Y*-band spectra for the three secure LAE detections, with the 1D spectrum above and corresponding 2D spectrum (matched in wavelength space) below for each source. Each 1D spectrum shows the Gaussian-smoothed signal as a blue solid line, the unsmoothed signal as a blue dashed line, the error spectrum in solid gray, and the Gaussian fit to the Lyα emission line in orange. Each panel lists the source ID, the Lyα-derived spectroscopic redshift, and the S/N of the Lyα detection for each source. In the 2D spectra, sky lines are marked with blue bars, and the location of the line both spatially and spectrally is marked with the dashed crosshairs. These Lyα detections are categorized as secure because both their spectra and SED fits are robust (see Section 3.2 for more details and Section 4 for individual source notes).

and have spectroscopic redshift solutions well-matched to the photometric redshift PDF(s). All secure sources also had average scores above 3.0/4.0 from the coauthor vetting survey, wherein a maximum score of 4.0 reflects the scenario wherein all 22 coauthors voted the source as "Secure." Tentative sources were so classified because their Lyα lines were lower S/N, their photometric redshift may not align well with the identified line, or some other reason that casts the security of the identification in doubt. Justification of placement in the secure or tentative subsample is described on a per-source basis below.

The *Y*-band spectra of the secure sample is shown in Figure 3, and the spectra of the tentative sample is shown in Figure 4. Redshift solutions for our 11 LAEs are found by Gaussian fit (rather than an asymmetric Gaussian as our signals are faint) to the centroid of the emission line, with no velocity offset applied. To derive redshifts, we adopt rest-frame Lyα wavelength of 1215.67 Å. Line fluxes are measured from the area under the best-fit Gaussian to the candidate Lyα emission line and uncertainties are calculated from error propagation on the best-fit parameters. We estimate 1σsensitivity ranging $\sim 2-5 \times 10^{-18}$ erg s^{-1} cm^{-2} in terms of line flux depth for the survey. Rest-frame equivalent widths (EWs) for each Lyα emission line are calculated by dividing the Lyα emission line flux ($F_{Ly\alpha}$) by $(1 + z_{Ly\alpha})$ times the rest-frame UV continuum flux density (derived from the average flux density of the best-fit SED within rest-frame 1230–1280 Å). Note that the EWs are derived using the combination of photometrically constrained continuum and line flux from our spectra; for this reason, we do not analyze the EWs of our detections in depth. Target information and redshifts are listed in Table 2, and the characteristics for each source are detailed further in Section 4.

4. Characterization of LAEs

4.1. Photometric Characterization

Photometric measurements are drawn from the deepest available catalog, which for the majority of our sample were the CANDELS catalogs (Grogin et al. 2011; Koekemoer et al. 2011;

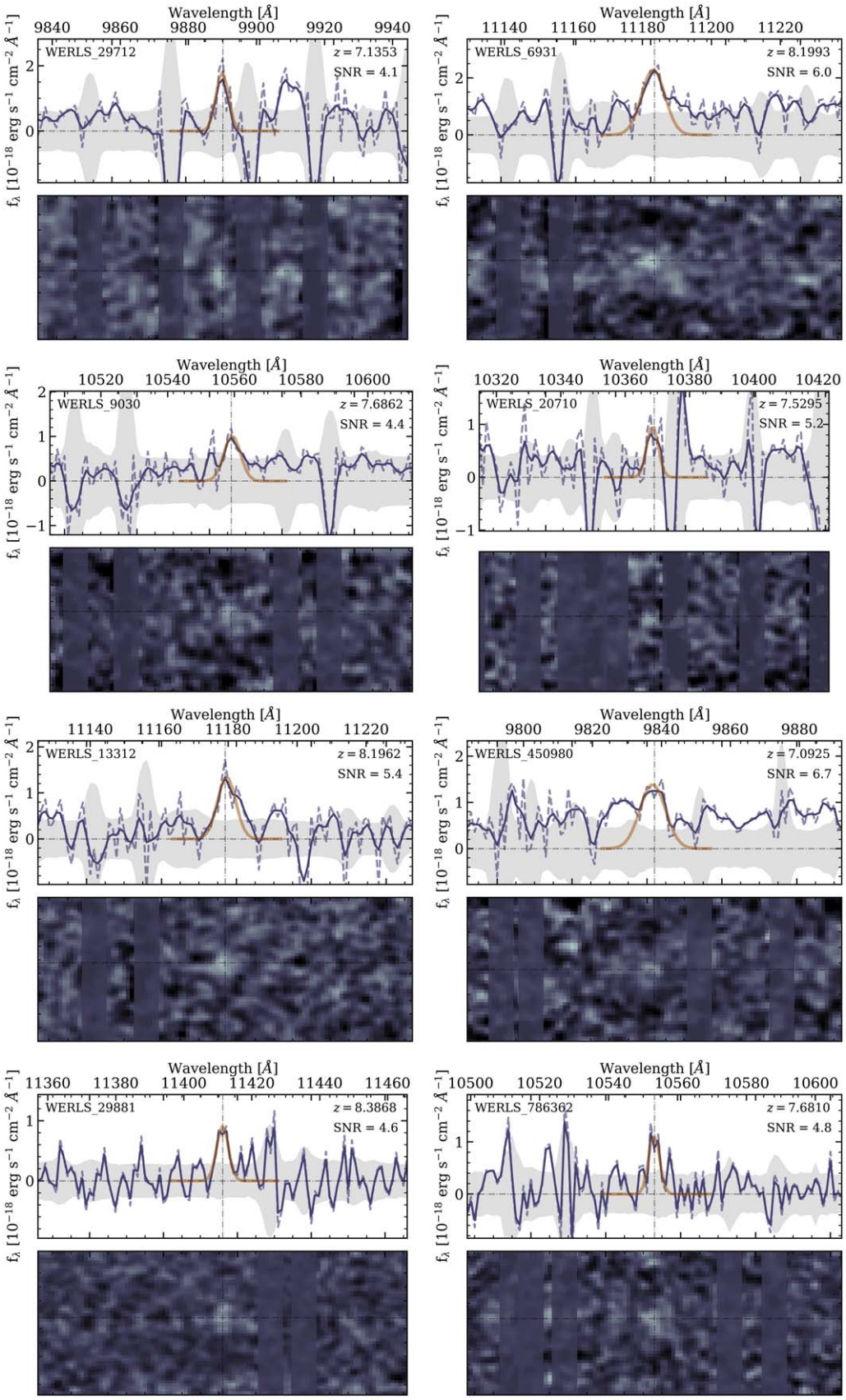

Figure 4. WERLS MOSFIRE *Y*-band spectra for the eight tentative LAE detections, with markers styled as in Figure 3. These Lyα detections are categorized as tentative because their spectra and/or line identifications are less robust than the secure detections (see Section 3.2 for more details and Section 4 for individual source notes).

Table 2
LAEs and Redshift Information

ID	R.A. J2000	Decl. J2000	Mask	$z_{\rm phot}$	$z_{\rm Ly\alpha}$	$F_{\rm Ly\alpha}$ 10^{-17} erg s^{-1} cm^{-2}	$EW_{\rm Ly\alpha}$ Å	S/N	Other Refs.
(1)	(2)	(3)	(4)	(5)	(6)	(7)	(8)	(9)	(10)
⋆SECURE LAES ⋆									
WERLS_72964	10:00:19.40	+02:29:36.64	wmmc06	$8.5^{+0.2}_{-0.7}$	7.8881	1.0 ± 0.4	7 ± 3	4.0	
WERLS_69492[a]	14:20:12.08	+53:00:26.82	wmme01	$7.8^{+0.2}_{-0.4}$	7.4763	1.4 ± 0.5	24 ± 10	7.7	RB16, S17, J22, J23
WERLS_32350[a]	14:19:59.77	+52:56:31.09	wmme01	$8.3^{+0.2}_{-1.3}$	7.5501	0.6 ± 0.5	11 ± 9	5.6	J22, J23
⋆TENTATIVE LAES ⋆									
WERLS_29712	02:17:06.97	–05:12:15.77	wmmu01	$6.8^{+0.1}_{-5.5}$	7.1353	1.2 ± 0.6	60 ± 30	4.1	
WERLS_6931	02:17:07.82	–05:08:35.09	wmmu01	$6.8^{+0.8}_{-5.3}$	8.1993	1.9 ± 0.4	160 ± 40	6.0	
WERLS_9030	10:00:24.79	+02:12:28.66	wmmc02	$7.0^{+0.4}_{-5.6}$	7.6862	0.69 ± 0.14	10 ± 2	4.4	
WERLS_20710	10:00:26.71	+02:15:47.20	wmmc02	$6.5^{+0.08}_{-4.8}$	7.5295	0.5 ± 0.5	20 ± 30	5.2	
WERLS_13312	10:00:27.42	+02:13:35.54	wmmc02	$8.1^{+0.1}_{-1.5}$	8.1962	0.9 ± 0.2	100 ± 40	5.4	
WERLS_786362	10:00:42.72	+02:20:58.85	wmmc05	$7.41^{+0.09}_{-0.12}$	7.6810	0.5 ± 0.2	170 ± 210	4.8	
WERLS_450980	10:00:45.58	+02:09:43.34	wmmc01	$7.3^{+0.1}_{-0.8}$	7.0925	1.3 ± 0.2	16 ± 3	6.7	
WERLS_29881	14:20:20.28	+53:00:31.28	wmme01	$6.4^{+0.4}_{-4.9}$	8.3868	0.40 ± 0.12	55 ± 20	4.6	

Notes. Columns: (1) WERLS object ID, (2) right ascension, (3) declination, (4) WERLS MOSFIRE mask for object, (5) peak EAZY photometric redshift and inner 68% uncertainty, (6) spectroscopic redshift measured from Lyα emission line, (7) Lyα emission line flux and uncertainty, (8) EW of Lyα emission line, (9) Lyα emission line detection S/N ratio, and (10) other literature works that report Lyα emission for the source, where RB16 = Roberts-Borsani et al. (2016), S17 = Stark et al. (2017), J22 = Jung et al. (2022), and J23 = Jung et al. (2024).
[a] Sources with secure multiline systemic redshifts from CEERS JWST/NIRSpec data.

Ashby et al. 2015). For one source in COSMOS that is not in the CANDELS catalog (WERLS_450980), we use COSMOS2020 photometry (Weaver et al. 2022). Only one source was in both the CANDELS and COSMOS2020 catalogs (WERLS_786362); however, this source also had JWST imaging available.

We search publicly available imaging from JWST (McElwain et al. 2023; Menzel et al. 2023; Rigby et al. 2023); at the time of writing, JWST/NIRCam imaging data (Rieke et al. 2023) existed for five sources: WERLS_9030, WERLS_20710, & WERLS_786362 in PRIMER-COSMOS, and WERLS_29712 & WERLS_6931 in PRIMER-UDS. Reduction of the PRIMER data was carried out as in M. Franco et al. (2024, in preparation). The raw NIRCam imaging in PRIMER-COSMOS was reduced with JWST Calibration Pipeline version Pipeline 1.10.0 (Bushouse et al. 2022), with the Calibration Reference Data System (CRDS)[30] pmap-1075, which corresponds to NIRCam instrument mapping imap-0252. For the imaging in PRIMER-UDS, we use the publicly available `grizli` reduction (Brammer 2023). From the reduced NIRCam imaging, we measure aperture photometry using `photutils` (Bradley et al. 2023) from images PSF homogenized to F444W (using `pypher`; Boucaud et al. 2016).

We recompute photometric redshift PDFs uniformly for our entire sample of LAEs in order to incorporate the new JWST data. We fit each galaxy SED with EAZY (Brammer et al. 2008), which computes linear combinations of predefined templates to derive photometric redshift probability distribution functions (PDFs) based on the χ^2 of the templates. Given that our sources are LAEs, we adopt the template set detailed in Larson et al. (2022), with the standard `tweak_fsps_QSF_12_v3` set of 12 FSPS (Conroy et al. 2010) and additional bluer LAE models, designed for high redshift star-forming galaxies such as those we target here. Specifically, we use Set 3: Reduced Lyα from Larson et al. (2022), which include models with emission lines added but with Lyα reduced to 1/10 of that produced by `CLOUDY` (Ferland et al. 2017) to emulate a 10% Lyα escape fraction, meant to represent typical $4 < z < 7$ galaxies. We allow the redshift to vary from $0.01 < z < 10.0$ with a step size of $\Delta z = 0.01$, and assume no redshift prior in order to derive the photometric redshift PDF. The results of these fits compared to the Lyα-derived spectroscopic redshifts are shown as subpanels in Figure 5 (for the secure sample) and in Figure 6 (for the tentative sample).

While sources were originally selected via photometric constraints derived from SED fitting, with new redshift constraints in hand from spectroscopy, we improve upon these SED characterizations using the Bayesian SED fitting code, `Bagpipes` (Carnall et al. 2018). For each source, we fix the redshift to the Lyα-derived spectroscopic redshift. Since we are able to fix the redshifts, we adopt a nonparametric star formation history (SFH) via the Leja et al. (2019) continuity SFH model. We adopt seven age bins, the most recent bin capturing the star formation rate (SFR) in the last 10 Myr and a maximum epoch of star formation at $z = 20$. We adopt the bursty continuity prior from Tacchella et al. (2022). We allow the metallicity to vary from $0.001 < Z/Z_{\odot} < 2.5$ with a log-uniform prior. We adopt a Calzetti (2001) dust attenuation law, and we allow the attenuation to vary from $0.001 < A_V < 3$ with a log-uniform prior. We also include a nebular component; `Bagpipes` uses the `CLOUDY` photoionization models (Ferland et al. 2017) to generate HII regions, and follows Byler et al. (2017) wherein total nebular emission is the sum of emission from HII regions of different ages. We allow the ionization parameter $\log U$ to vary from –4 to –1, with a Gaussian prior with $\mu, \sigma = (-2, 0.25)$.

From the best-fit `Bagpipes` model, we calculate the absolute UV magnitude ($M_{\rm UV}$) of each source (listed in Table 2). The distribution of $M_{\rm UV}$ versus best available redshift for the sample is shown in Figure 7. Our targets are UV-bright by selection, but span a wide range of UV magnitude, with our spectroscopic sample spanning $-23.14 \leqslant M_{\rm UV} \leqslant -19.81$.

We derive physical properties from the best-fit `Bagpipes` model for each source (note that the following excludes values

[30] jwst-crds.stsci.edu

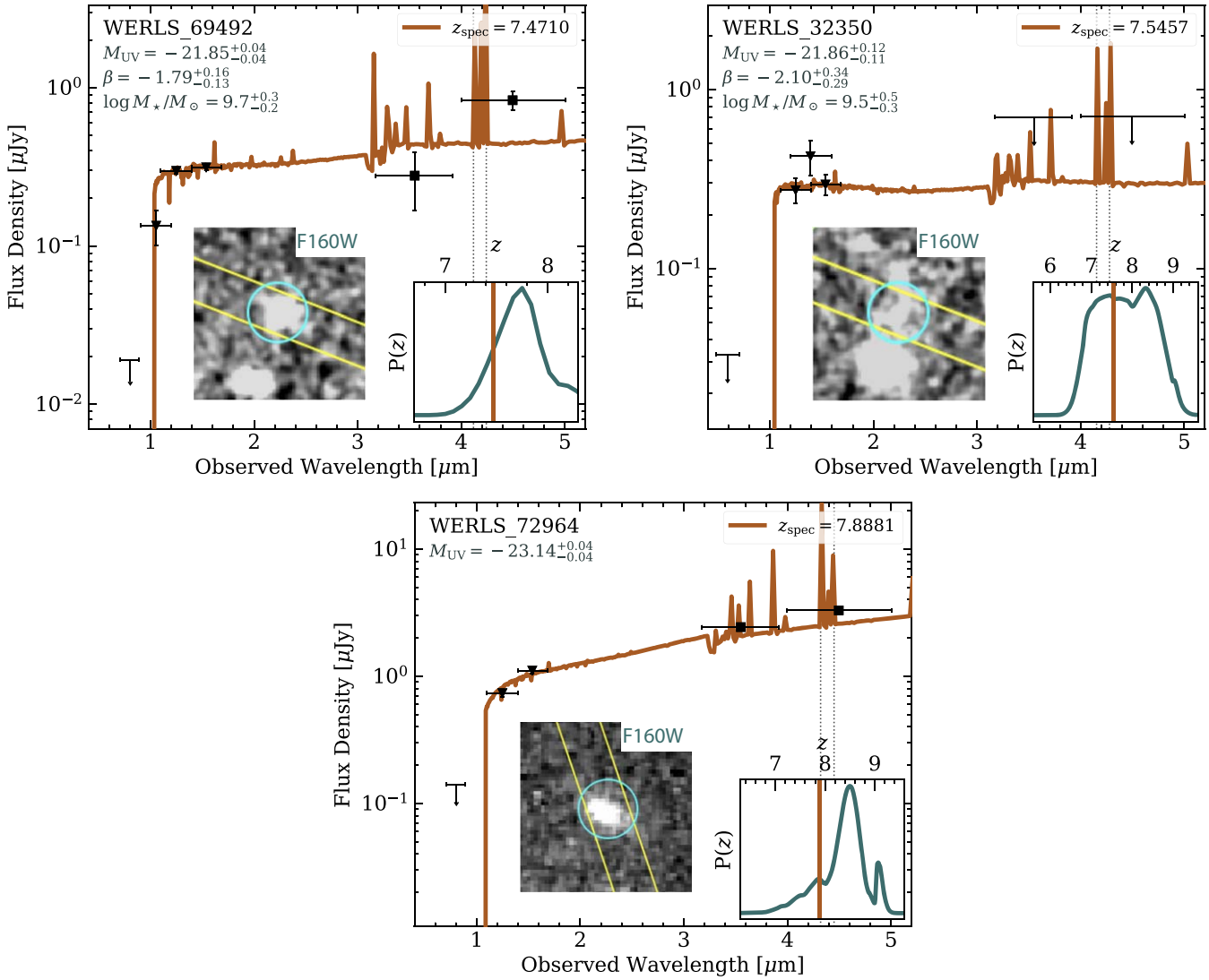

Figure 5. SED fits, image cutout, and photometric redshift PDF for each source in the secure sample. Each primary figure shows the best-fit `Bagpipes` SED fixed to the spec-z in orange and the photometry in black markers, noted by their instruments wherein circles are ground-based data, triangles are HST data, hexagons are JWST data, and squares are Spitzer data. The wavelength of redshifted [O III]/Hβ is marked with dotted lines. Inset on the left-hand side shows a 3" cutout (HST/F160W), overlaid with the MOSFIRE slit in yellow and the target in cyan. Inset on the right-hand side of each primary figure is the EAZY photometric redshift PDF in teal (allowing the redshift to vary), compared to the spectroscopic redshift solution in orange.

listed for WERLS_786362, which are not derived from the best-fit model to the photometry, but instead are taken directly from the generated `Bagpipes` model). As expected for LAEs, our galaxies are generally star-forming but show a broad range, with SFRs ranging 0.1-90 $M_\odot$ yr^{-1} and a median SFR of 10 $M_\odot$ yr^{-1}. We estimate a median stellar mass of $\sim 2.3 \times 10^9$ $M_\odot$ and ranging $8.5 < \log\,(M_\star/\,M_\odot) < 9.7$, suggesting our sample represents massive EoR galaxies but not necessarily the most extreme at this epoch. Given their Lyα detections and implied ionized photon escape, we expect these galaxies to be fairly blue; this is supported by their measured rest-frame UV slopes (β), ranging $-2.6 < \beta < -1.6$ with a median of $\beta \sim -2.1$. The measured properties for the sample are listed in Table 3.

4.2. Individual Sources

In the following subsections, we detail the spectroscopic and photometric analysis and properties for each source, and use this to justify their placement in the secure or tentative subsample.

4.2.1. WERLS_72964

WERLS_72964 is on mask wmmc06 with a S/N = 4.0 Lyα emission line corresponding to z_{spec} =7.8881, and is in our secure sample, with Lyα line flux of $F_{Ly\alpha}$ =$(1.0 \pm 0.4) \times 10^{-17}$ erg s^{-1} cm^{-2}. It lies within the COSMOS CANDELS coverage, is not in the COSMOS2020 catalog, and lies outside of PRIMER-COSMOS. We fit the target's CANDELS photometry (ID: 72964) and find a photometric redshift consistent with the spectroscopic solution within uncertainty, with z_{phot} =$8.5^{+0.2}_{-0.7}$. Furthermore, the source is detected significantly in IRAC Channel 1 (3.6 μm) and Channel 2 (4.5 μm), with some photometric excess (0.33 mag) in Channel 2 where there should be contamination from [O III]+Hβ nebular emission at both the spectroscopic and photometric redshift solutions. Coauthor vetting resulted in a score of 3.4/4 (a maximum score of 4 reflects the scenario wherein all 22 coauthors voted the source as secure). Given that the measured line flux is fairly high, the source's spectroscopic and photometric redshifts are consistent within uncertainties, the source shows some IRAC excess consistent with

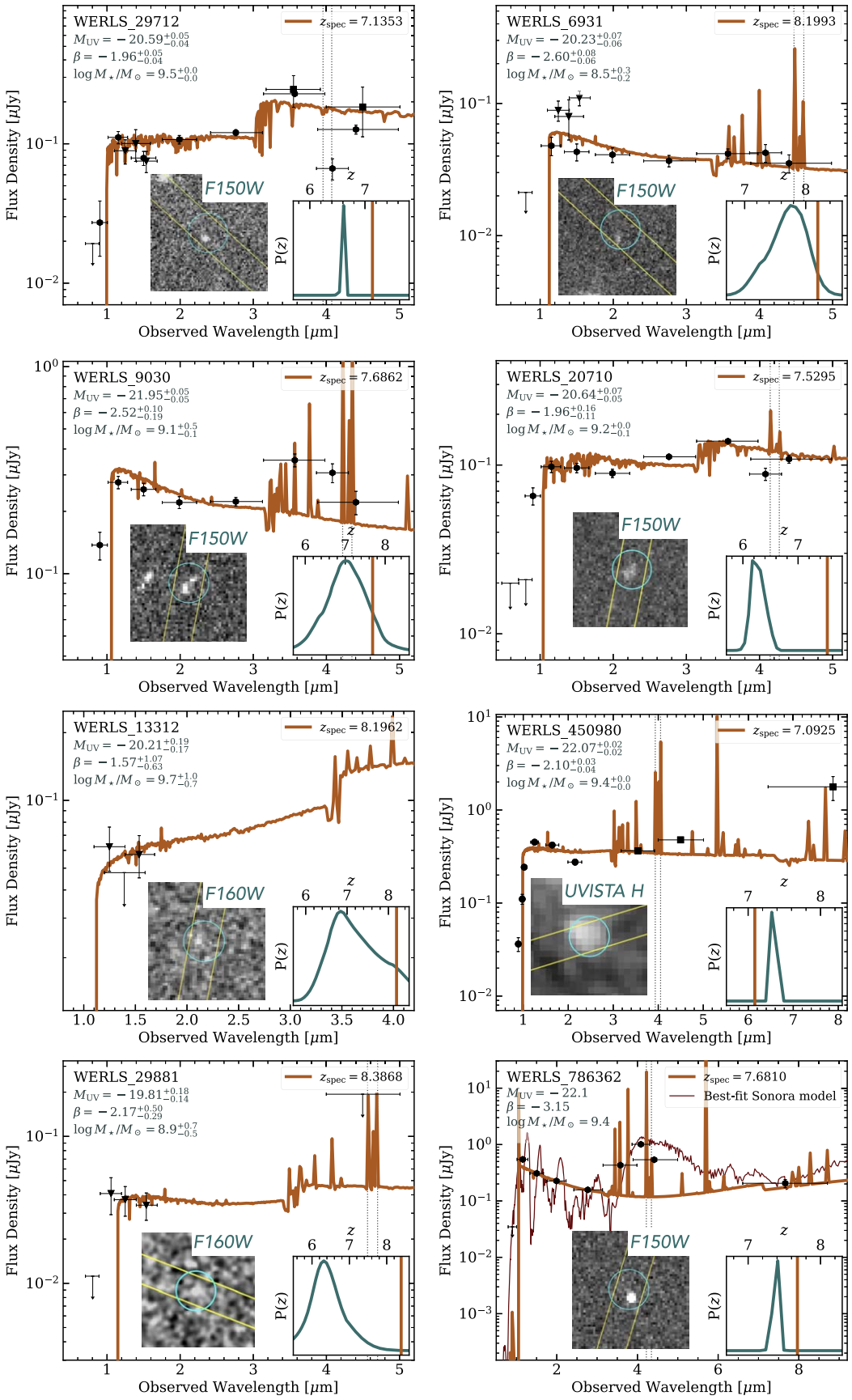

Figure 6. SED fits, image cutout, and photometric redshift PDF for each source in the tentative sample, with format consistent with Figure 5. WERLS_786362 also shows the best-fit Sonora brown dwarf model in thin red (see Section 4.2.4 for more details). Here, the cutouts are UltraVISTA/H, HST/F160W, or JWST/F150W as available.

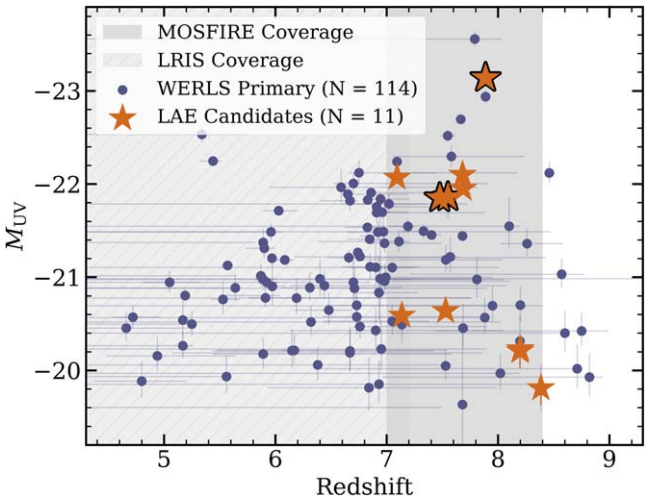

Figure 7. M_{UV} vs. redshift for all galaxies targeted in our MOSFIRE observations. Blue points denote all WERLS Primary targets (here, observed with MOSFIRE but selected for both LRIS and MOSFIRE wavelength ranges) and orange stars show the LAEs reported in this paper (black outlines highlight the secure subsample). Redshifts are photo-z's except for the LAEs, which have Lyα-derived spectroscopic redshifts as reported in this paper. Our targets are selected to be UV-bright—91% of the sample have $M_{UV} \leqslant -20$—but span a wide range of M_{UV}. The ranges of redshifted Lyα emission accessible with MOSFIRE Y-band and LRIS are represented as gray regions.

the redshift solution, and from a holistic review of the data, the coauthors rated the detection secure overall, we place this source in our secure sample.

4.2.2. WERLS_69492 a.k.a EGS-zs8-2

WERLS_69492 is a known LAE, first reported as EGS-zs8-2 in Roberts-Borsani et al. (2016), who detect Lyα at 4.7σ with MOSFIRE and measure a redshift of z_{spec} =7.4777; this observation is later supported by Stark et al. (2017), who report a 7.4σ Lyα detection for the target. It is in our secure sample and is our highest S/N Lyα detection, with S/N = 7.7, with Lyα line flux of $F_{Ly\alpha} = (1.4 \pm 0.5) \times 10^{-17}$ erg s^{-1} cm^{-2}. This line flux is consistent with the measurement from Roberts-Borsani et al. (2016) of $F_{Ly\alpha} = (1.6 \pm 0.3) \times 10^{-17}$ erg s^{-1} cm^{-2}, but is inconsistent with measurements in Jung et al. (2024), who find a $\sim$3 × higher flux with MOSFIRE and a $\sim$3 × lower flux with JWST/NIRSpec than our MOSFIRE measurement. Indeed, Jung et al. (2024) find a $\sim$5 × discrepancy between their measurements with MOSFIRE and NIRSpec, which they attribute primarily to significant slit losses in NIRSpec observations. We attribute differences in MOSFIRE line fluxes to differences in line fitting because we adopt a symmetric Gaussian here for lack of sufficient S/N to do a more sophisticated fit. The target is on mask wmme01 in the EGS field and is covered by CANDELS (ID: 69492) but does not fall in the CEERS JWST/NIRCam coverage. We fit the CANDELS photometry and find a photometric redshift of $z_{phot} = 7.8^{+0.2}_{-0.4}$, consistent within uncertainty with our Lyα-derived z_{spec} = 7.4763. For this spectroscopic redshift as with all of our Lyα-derived redshifts, we adopt a rest-frame Lyα wavelength of 1215.67 Å. We attribute the small difference between our derived redshift and previously reported spectroscopic redshifts to differences in fitting method, namely fitting to the blue side versus Gaussian peak. As we describe in Section 3.2, we opt to measure at the Gaussian peak given the S/N and resolution of our detections. The `Bagpipes` SED fit suggests excess from nebular emission, which is supported by the strong photometric excess in IRAC Channel 2 (4.5 μm) of 1.19 mag (corroborated by Roberts-Borsani et al. 2016). Coauthor vetting resulted in a score of 3.8/4.

The target was also observed by CEERS with JWST/NIRSpec (MSA ID: 698) with medium resolution in the G140M, G235M, and G395M filters. The CEERS reduction confirms the redshift of the source via multiple strong, rest-frame optical emission lines (including [O III]+Hβ), with $z_{spec} = 7.4710$ (Jung et al. 2024). We attribute the small $\Delta z = 0.005$ between spectroscopic redshift solutions to the expected velocity offset between Lyα and the systemic redshift. Here, Lyα emission is redshifted from the rest-frame optical emission with a velocity offset of $\Delta v \sim 188$ km s^{-1}, consistent within uncertainty with the measured velocity offset in Jung et al. (2024) of 142 ± 142 km s^{-1}. Given that the Lyα detection is confirmed by multiple independent data sets and analyzes including via multiline spectroscopic confirmation with JWST/NIRSpec, we place this source in our secure sample.

4.2.3. WERLS_32350

WERLS_32350 is on mask wmme01 with a S/N = 5.6 Lyα emission line corresponding to z_{spec} = 7.5501 and is in our secure sample, with Lyα line flux of $F_{Ly\alpha} = (0.6 \pm 0.5) \times 10^{-17}$ erg s^{-1} cm^{-2}, consistent with the line flux measurement in Jung et al. (2024) within uncertainties, though theirs was derived from JWST/NIRSpec data. Differences in exact line flux measurements between instruments are expected, especially given that the line falls partially on a sky line, which impacts our ground-based observations. It is selected from EGS CANDELS (ID: 32350) and is not within the CEERS JWST/

Table 3
`Bagpipes`-derived Galaxy Properties

ID	M_{UV} ABmag	β	SFR $M_\odot$ yr^{-1}	$M_\star$ Log $M_\odot$
(1)	(2)	(3)	(4)	(5)
WERLS_72964	$-23.14^{+0.04}_{-0.04}$	…[a]	…[a]	…[a]
WERLS_69492[c]	$-21.85^{+0.04}_{-0.04}$	$-1.79^{+0.16}_{-0.13}$	90^{+40}_{-20}	$9.7^{+0.3}_{-0.2}$
WERLS_32350[c]	$-21.86^{+0.12}_{-0.11}$	$-2.1^{+0.3}_{-0.3}$	40^{+50}_{-20}	$9.5^{+0.5}_{-0.3}$
WERLS_29712	$-20.59^{+0.05}_{-0.04}$	$-1.96^{+0.05}_{-0.04}$	$0.1^{+0.4}_{-0.1}$	$9.5^{+0.3}_{-0.3}$
WERLS_6931	$-20.23^{+0.07}_{-0.06}$	$-2.6^{+0.08}_{-0.06}$	4^{+1}_{-1}	$8.5^{+0.3}_{-0.2}$
WERLS_9030	$-21.95^{+0.05}_{-0.05}$	$-2.5^{+0.1}_{-0.2}$	24^{+5}_{-18}	$9.1^{+0.5}_{-0.1}$
WERLS_20710	$-20.64^{+0.07}_{-0.05}$	$-1.96^{+0.16}_{-0.11}$	10^{+7}_{-4}	$9.2^{+0.1}_{-0.1}$
WERLS_13312	$-20.21^{+0.19}_{-0.17}$	$-1.6^{+1.1}_{-0.6}$	10^{+70}_{-10}	$9.7^{+1.0}_{-0.7}$
WERLS_786362	-22.1[b]	-3.15[b]	…[b]	9.4[b]
WERLS_450980	$-22.07^{+0.02}_{-0.02}$	$-2.10^{+0.03}_{-0.04}$	65^{+5}_{-5}	$9.4^{+0.1}_{-0.1}$
WERLS_29881	$-19.81^{+0.18}_{-0.14}$	$-2.2^{+0.5}_{-0.3}$	5^{+9}_{-4}	$8.9^{+0.7}_{-0.5}$

Notes. Columns: (1) WERLS object ID, (2) UV magnitude, (3) UV slope (β), (4) SFR, and (5) stellar mass ($M_\star$). All properties and inner 68% uncertainties are derived from best-fit `Bagpipes` SED fits.

[a] WERLS_72964 has blended IRAC photometry, and therefore we do not report physical properties for the source given its contaminated infrared photometry.

[b] Estimated properties apply if WERLS_786362 is indeed an EoR galaxy and not a brown dwarf; we are unable to constrain a physically plausible SFR and do not report uncertainties because properties are taken directly from a generated galaxy model rather than estimated from a best-fit model to the data (see Section 4.2.4. for more details).

[c] Sources with secure multiline systemic redshifts from CEERS JWST/NIRSpec data.

NIRCam coverage. We fit the CANDELS photometry and find a photometric redshift of $z_{\rm phot} = 8.3^{+0.2}_{-1.3}$, consistent within uncertainty with our Lyα-derived $z_{\rm spec} = 7.5501$. The Bagpipes SED fit suggests excess from [O III]+Hβ nebular emission, which is supported by the strong photometric excess in IRAC Channel 2 (4.5 μm) of 0.91 mag. Coauthor vetting resulted in a score of 3.0/4.

The target has multiple MOSFIRE *Y*-band observations, through this program and in Jung et al. (2022), who report a Lyα detection at $z = 7.7759 \pm 0.0012$ (ID: z8_32350), inconsistent with our $z = 7.5501$ Lyα detection, which was likely not discovered in the Jung et al. (2022) automated line search because it partially overlaps with a sky line and was excluded in their automated search. The target was observed by CEERS with JWST/NIRSpec (MSA ID: 689) with medium resolution in the G140M, G235M, and G395M filters. The CEERS reduction confirms the redshift of the source via multiple strong, rest-frame optical emission lines (including [O III] +Hβ), with $z_{\rm spec} = 7.5457 \pm 0.0001$ (Jung et al. 2024). This is consistent with the WERLS Lyα-derived redshift, with a small Δz between this spectroscopic redshift solutions to the expected offset between systemic and Lyα-derived redshifts. In Jung et al. (2024), the authors re-analyze their MOSFIRE data of the source and measure a Lyα-derived redshift of $z_{\rm spec} = 7.552 \pm 0.003$, consistent with our Ly$\alpha$ redshift; we attribute the small difference in our measurements to differences in fitting method, wherein we adopt the Gaussian peak as noted in Section 3.2. The measured velocity offset of Lyα is $\Delta v \sim 154\,{\rm km\,s^{-1}}$, with Ly$\alpha$ emission redshifted from rest-frame optical emission, consistent within uncertainty with the measured velocity offset in Jung et al. (2024) of $221 \pm 109\,{\rm km\,s^{-1}}$. While the candidate Ly$\alpha$ emission line overlaps partially with a sky line in our spectra and the measured line flux is somewhat faint, the source has been confirmed via multiline spectroscopic confirmation with JWST/NIRSpec, so we place it in our secure sample.

4.2.4. WERLS_786362

WERLS_786362 is on mask wmmc05 and has a S/N = 4.8 Lyα emission line corresponding to $z_{\rm spec} = 7.6810$, with Lyα line flux of $F_{{\rm Ly}\alpha} = (0.5 \pm 0.2) \times 10^{-17}\,{\rm erg\,s^{-1}\,cm^{-2}}$. It lies within the COSMOS CANDELS coverage and within PRIMER-COSMOS. This source was imaged by both NIRCam and MIRI with PRIMER, and has a faint detection in MIRI/F770W. We fit the target's JWST+HST photometry (CANDELS ID: 786362) and find a best-fit SED with $z_{\rm phot} = 7.41^{+0.09}_{-0.12}$, consistent with the spectroscopic solution. Coauthor vetting resulted in a score of 3.6/4.

The photometry for WERLS_786362 demonstrates a particularly blue slope at short wavelengths in addition to a red slope at long wavelengths (specifically, it is very blue in F115W−F200W and red in F277W−F444W), which could be indicative of a brown dwarf (e.g., Langeroodi et al. 2023; Burgasser et al. 2024; Hainline et al. 2024). Its compact morphology, akin to the "little red dots" discovered recently in *JWST* images, is consistent with both a high redshift galaxy or a brown dwarf. We fit the photometry to a generated Bagpipes galaxy model with a very blue component with boosted Lyα and a red dusty component with boosted Hβ, as well as a brown dwarf with $T = 1000$ K and $\log g = 3.0$ from the Sonora models (Marley et al. 2021), and find that both models plausibly match the data. Given that our Bagpipes galaxy model is physically extreme, the photometric evidence suggests the brown dwarf case is more likely. However, the brown dwarf solution does not account for the strong emission line we detect with MOSFIRE, which supports the high redshift galaxy case assuming that the line is Lyα. Since we lack multiline confirmation of the source, and therefore are unable to distinguish between the brown dwarf and high redshift LAE cases, we place this source in our tentative sample.

4.2.5. WERLS_29712

WERLS_29712 has a candidate Lyα line at S/N = 4.1 with $z_{\rm spec} = 7.1353$, with Lyα line flux of $F_{{\rm Ly}\alpha} = (1.2 \pm 0.6) \times 10^{-17}\,{\rm erg\,s^{-1}\,cm^{-2}}$. It is on mask wmmu01 in the UDS field. We fit the target's UDS CANDELS (ID: 29712) and PRIMER-UDS photometry and find $z_{\rm phot} = 6.8^{+0.1}_{-5.5}$, with a small peak in the photometric redshift PDF at $z \sim 1$–2, and 9% of the total PDF at $z < 3$. Coauthor vetting resulted in a score of 2.9/4. This lower-redshift solution is inconsistent with the spectroscopic solution; given this discrepancy along with the faint signal in the 2D spectrum, we place it in the tentative sample.

4.2.6. WERLS_6931

WERLS_6931 has a candidate Lyα line with S/N = 6.0, corresponding to $z_{\rm spec} = 8.1993$, with Lyα line flux of $F_{{\rm Ly}\alpha} = (1.9 \pm 0.4) \times 10^{-17}\,{\rm erg\,s^{-1}\,cm^{-2}}$. It is on mask wmmu01 in the UDS field. We fit the target's CANDELS (ID: 6931) and PRIMER-UDS photometry and find $z_{\rm phot} = 6.8^{+0.8}_{-5.3}$, with a peak in the photometric redshift PDF at $z \sim 1$–2, and 24% of the total PDF at $z < 3$. Coauthor vetting resulted in a score of 2.7/4. While the $z_{\rm spec}$ solution falls within the broader high redshift peak of the photometric redshift PDF, given that only 35% of the redshift PDF is at $z > 7$, we place it in the tentative sample.

4.2.7. WERLS_9030

WERLS_9030 is on mask wmmc02 and has a moderate Lyα emission line candidate detection at S/N = 4.4 corresponding to $z_{\rm spec} = 7.6862$, with Lyα line flux of $F_{{\rm Ly}\alpha} = (0.69 \pm 0.14) \times 10^{-17}\,{\rm erg\,s^{-1}\,cm^{-2}}$. It lies within the COSMOS CANDELS and PRIMER-COSMOS coverage, and is not in the COSMOS2020 catalog. This source was imaged by both NIRCam and MIRI with PRIMER, and has a faint detection in MIRI/F770W. We fit the target's CANDELS (ID: 9030) and PRIMER photometry, and find a photometric redshift solution of $z_{\rm phot} = 7.0^{+0.4}_{-5.6}$, consistent with the spectroscopic solution within errors, with a smaller peak in the photometric redshift PDF at $z \sim 1$–2, and 22% of the total PDF at $z < 3$. This lower-redshift solution is inconsistent with the spectroscopic solution; fixing the SED to the $z_{\rm spec}$ returns a solution wherein the F814W flux is partially contaminated by Lyα emission, which is consistent with its MOSFIRE spectrum. Coauthor vetting resulted in a score of 2.8/4. Since the Lyα line is fairly faint in the 2D spectrum, we place it in the tentative sample.

4.2.8. WERLS_20710

WERLS_20710 is on mask wmmc02 and has a moderately detected (S/N = 5.2) Lyα emission line candidate corresponding to $z_{\rm spec} = 7.5295$, with Lyα line flux of $F_{{\rm Ly}\alpha} = (0.5 \pm 0.5) \times 10^{-17}\,{\rm erg\,s^{-1}\,cm^{-2}}$. It lies within the COSMOS CANDELS coverage and within PRIMER-COSMOS. Coauthor vetting resulted in a score of 2.7/4. We fit the target's JWST+HST

photometry (CANDELS ID: 20710) and find a photometric redshift of $z_{\rm phot}$ $=6.5^{+0.08}_{-4.8}$, somewhat inconsistent with the spectroscopic solution; given this, we place this source in our tentative sample.

4.2.9. WERLS_13312

WERLS_13312 is on mask wmmc02 and has a moderately detected (S/N=5.4) Lyα emission line candidate corresponding to $z_{\rm spec} = 8.1962$, with Lyα line flux of $F_{{\rm Ly}\alpha} = (0.9 \pm 0.2) \times 10^{-17}$ erg s^{-1} cm^{-2}. It lies within the COSMOS CANDELS coverage but not in PRIMER-COSMOS or COSMOS-Web, and is not in the COSMOS2020 catalog. We fit the target's CANDELS photometry (ID: 13312) and find a best-fit SED with $z_{\rm phot}$ $=8.1^{+0.1}_{-1.5}$, consistent with the spectroscopic solution. However, the SED appears poorly constrained given that the target is undetected in *Y*-band and bluer and is not detected in IRAC. Coauthor vetting resulted in a score of 3.2/4. Though the line was highly ranked by coauthors, given its dearth of secure multiband photometry and the absence of clear negative signal in the 2D spectrum, we place this source in our tentative sample.

4.2.10. WERLS_450980

WERLS_450980 is selected from the COSMOS2020 catalog, is on mask wmmc01, and is in our tentative sample. It has candidate Lyα emission detected at S/N = 6.7, giving $z_{\rm spec}$ $=7.0925$, with Lyα line flux of $F_{{\rm Ly}\alpha}$ $=(1.3 \pm 0.2) \times 10^{-17}$ erg s^{-1} cm^{-2}. There is a much fainter positive signal with S/N = 3.9 just blueward of the candidate emission line; this could indicate the signal is the [O II] doublet rather than Lyα. Assuming the brighter emission line candidate is [O II] with rest-frame wavelength 3729 Å, that would place the source at $z = 1.639$, and we would expect to find the rest-frame 3727 Å emission line ∼6 Å blueward. Here, the fainter signal is nearly twice that separation, at ∼11 Å from our candidate emission line. Therefore, we find the Lyα line identification to be more likely. Using the COSMOS2020 photometry (ID: 450980), we find the photometric redshift to be well-matched to the spectroscopic solution, with $z_{\rm phot}$ $=7.3^{+0.1}_{-0.8}$. Coauthor vetting resulted in a score of 2.7/4. While the line appears real and the SED results are consistent with our Lyα-derived spectroscopic solution, we include the source in the tentative sample due to the uncertainty in our line identification.

4.2.11. WERLS_29881

WERLS_29881 is in our tentative sample and is our highest redshift LAE, detected at S/N = 4.6 with $z_{\rm spec}$ $= 8.3868$, with Lyα line flux of $F_{{\rm Ly}\alpha} = (0.40 \pm 0.12) \times 10^{-17}$ erg s^{-1} cm^{-2}. It is on mask wmme01 in the EGS field, but lies outside of the CEERS coverage. We fit the target's CANDELS photometry (ID: 29881) and find a best-fit SED with $z_{\rm phot} = 6.4^{+0.4}_{-4.9}$, with a smaller peak in the photometric redshift PDF at $z \sim 1$, and 10% of the total PDF at $z < 3$. This is inconsistent with the spectroscopic solution; fixing the SED to the $z_{\rm spec}$ returns a solution wherein the HST/F814W flux is partially contaminated by Lyα emission, which is consistent with its MOSFIRE spectrum. Furthermore, while the source is undetected in IRAC Channel 1 (3.6 μm), it is detected in IRAC Channel 2 (4.5 μm), where there should be contamination from [O III] +Hβ nebular emission at the spectroscopic redshift. Coauthor vetting resulted in a score of 3.3/4. While coauthors ranked this detection highly, given the line detection is at the edge of the MOSFIRE wavelength coverage, it is statistically more likely to be noise and we place it in the tentative sample.

4.3. JWST/NIRSpec Observations

Five of our primary targets in the EGS/CEERS field were observed with JWST/NIRSpec (Böker et al. 2023) as part of the CEERS program: WERLS_69492, WERLS_32350, WERLS_35089, WERLS_45153, and WERLS_40898. For two of these five sources (WERLS_69492 and WERLS_32350), the NIRSpec data secures the WERLS Lyα-derived redshift, anchored by strong nebular emission lines in the near-infrared, namely [O III] and Hβ (see Sections 4.2.2. and 4.2.3. for more details). For the other three sources, we did not identify Lyα emission in the WERLS MOSFIRE data, explained for each source in more detail below.

MOSFIRE Primary target WERLS_40898 is on mask wmme03 in the EGS field and had no Lyα detection in the WERLS MOSFIRE data. It was observed by CEERS with JWST/NIRSpec (MSA ID: 1027) with both PRISM mode and with medium resolution in the G140M, G235M, and G395M filters. As reported in Arrabal Haro et al. (2023), the CEERS reduction secures the redshift of the source via multiple strong, rest-frame optical emission lines (including [O III]+Hβ), with $z_{\rm spec}$ $=7.820^{+0.001}_{-0.001}$ (see also Heintz et al. 2023; Sanders et al. 2024). The medium resolution spectrum also shows strong Lyα emission at 10732.1 Å, and Tang et al. (2023) find a fairly large Lyα velocity offset from the systemic redshift of ∼323 km s^{-1}. Based on the strength of the NIRSpec detection, we expect Lyα to be detectable by WERLS for this source. However, the spectrum is contaminated by a sky line at the observed Lyα wavelength. Additionally, mask wmme03 was less than half complete, with only eight ABBA sequences taken (out of our goal of 20+ sequences or about 4 hr of total exposure time).

WERLS_35089 is a MOSFIRE Primary target on mask wmme01 in the EGS field and had no Lyα detection in the WERLS MOSFIRE data, corroborated by the MOSFIRE *Y*-band nondetection in Jung et al. (2022). It was observed by CEERS with JWST/NIRSpec (MSA ID: 716) with PRISM mode only. The CEERS reduction shows a single bright emission line, which given photometric redshift priors can be identified securely as Hα, with $z_{\rm spec}$ $= 6.959$ (P. Arrabal Haro et al. 2024, in preparation); the redshift is also consistent with [O III] falling in the detector gap for these observations. While there is no detectable Lyα emission line in the spectrum, the Lyα break is detected, which anchors the spectroscopic redshift solution.

WERLS Primary target WERLS_45143 is on mask wmme01 in the EGS field and had no Lyα detection in the WERLS MOSFIRE data. It was observed by CEERS with JWST/NIRSpec (MSA ID: 717) with both PRISM mode and with medium resolution in the G140M, G235M, and G395M filters. The CEERS reduction secures the redshift of the source via multiple strong emission lines (including [O III]+Hβ as well as Hα), with $z_{\rm spec}$ $= 6.934$ (P. Arrabal Haro et al. 2024, in preparation). The NIRSpec spectrum shows no Lyα emission, but the Lyα break is detected.

5. Discussion

The primary aims of the WERLS experiment in its entirety are to (1) conduct a census of Lyα emission in known, luminous EoR galaxy candidates to map ionization bubbles in

the IGM on scales larger than their expected size, (2) directly compare the Lyα-inferred location of ionized bubbles to underlying galaxy density maps to be measured via deep JWST/NIRCam imaging to directly constrain the environments of LAEs, related to the drivers of reionization, and (3) increase the number of spectroscopically confirmed bright EoR sources to inform photometric redshift calibration of fainter EoR galaxies exclusively detected by JWST. This paper (in part) addresses the first and third aims by reporting new Lyα detections for bright galaxies at $z \sim 7$–8. Here, we discuss the efficacy of this census of Lyα and look ahead to future efforts to address the latter goals of the WERLS experiment.

5.1. Observed LAE Yield

In order to assess the survey yield, we first consider the completeness of our observed subsample compared to the parent WERLS sample. We run Kolmogorov–Smirnov (K-S) tests (Massey 1951) on our sample, and confirm that the distributions of magnitudes and photometric redshifts for the observed sample are consistent with the parent sample. We limit these tests to the MOSFIRE Primary targets for both the parent sample and observed subsample because pointing positions and positions on the sky were driven by these targets. We find no direct bias in terms of magnitudes or photometric redshifts of targeted versus parent sample. This follows expectations given that source density was the primary way in which targets were selected.

Given that we lack spectroscopic redshifts for the majority of our primary targets, the photometric redshift accuracy can also impact our yield estimations. For our spectroscopic subsample, we find a mean $\Delta z/(1+z) = 0.04$. This is consistent with the photometric redshift accuracy of 5% reported for sources with comparable magnitudes in the COSMOS2020 catalog (Weaver et al. 2022). Furthermore, our accuracy is comparable to that of similar high redshift subsamples; for example, Pentericci et al. (2018) find $\Delta z/(1+z) = 0.07$ for their CANDELS-selected $z > 6.8$ spectroscopic sample.

To estimate the expected LAE yield for our observations, we consider the photometric redshift PDFs for the entire subsample of WERLS Primary targets ($N = 114$), the portion of the spectra that are blocked by OH sky lines, and the expected neutral fraction at $z \sim 7$–8 that would further reduce the number of observable LAEs. To compare these estimates to our observed sample of LAEs ($N = 11$), we separate out the MOSFIRE Primary targets ($N = 33$), which have photometric redshift solutions that peak strongly at $z \sim 7$–8 where Lyα is detectable in our data, and the other WERLS Primary (LRIS and MOSFIRE+LRIS) targets ($N = 27$ and $N = 54$, respectively), which have broader photometric redshift solutions within the EoR and/or are LRIS Primary targets at $z \lesssim 7$. For each subset and the total Primary target sample, we find the total photometric redshift cumulative distributions and use this to quantify the number of targets that would fall in the Lyα redshift range detectable for our observations. This quantity is then multiplied by the typical fraction of the spectrum that is contaminated by sky lines, ~38%, assuming an uncertainty of $\pm$10% to account for variation both in the exact wavelength coverage of each spectrum and in the seeing (and therefore width of the sky lines). Finally, we multiply this number by the fraction of the IGM that is ionized at our target epoch; given that our observations do not directly constrain the ionized fraction, we allow it to vary. Importantly, the Lyα fraction that we consider here is not equal to the IGM neutral fraction because the neutral fraction also depends on Lyα velocity offsets and ionized bubble sizes. We do not attempt to constrain the neutral fraction here and apply a varying average neutral fraction (which should broadly contain the variations due to velocity offsets and ionized bubbles) to serve as an upper limit for our LAE yield estimation.

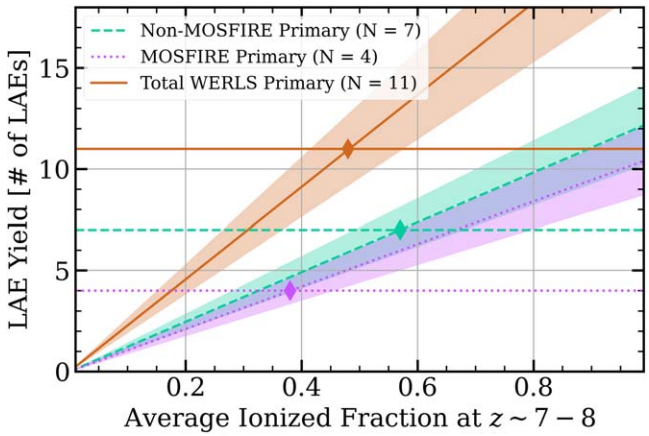

Figure 8. LAE yield for our MOSFIRE observations vs. ionized fraction (horizontal lines) compared to the expected detection rate given the photometric redshift PDFs for our targets and portion of the spectrum blocked by sky lines. The MOSFIRE Primary sample (targets most likely at $z \sim 7$–8) is shown in purple, the NonMOSFIRE WERLS Primary sample (drawn from a broader redshift range within the EoR) is shown in cyan, and the total WERLS Primary sample is in orange. The uncertainty on sky line contamination is represented by the shaded regions. Our total LAE yield ($N = 11$) supports the scenario wherein reionization is at its midpoint at $z \sim 7$–8.

Our expected LAE yield as a function of the average cosmic ionized fraction is shown in Figure 8. We detect $N = 7$ NonMOSFIRE Primary targets and $N = 4$ MOSFIRE Primary targets, for a total of 11 LAEs. None of our 11 LAEs were LRIS Primary targets, but the subsample did contain MOSFIRE Primary and both MOSFIRE+LRIS Primary targets. Given this, we can estimate the yield simply by taking the number of detected LAEs ($N = 11$) over the number of targeted candidates from the two primary categories (MOSFIRE, $N = 33$ and MOSFIRE+LRIS, $N = 54$), for a ~13% yield of Lyα emission observed from our EoR targets. This is broadly consistent with expectations for a Universe that is half-ionized at $z \sim 7$–8 (see Figure 8) and demonstrates the relative success of WERLS at detecting Lyα in UV-bright EoR galaxies.

5.2. Possible Ionized Bubble at z = 7.68

Observing Lyα emission at $z \sim 7$–8 is fairly unlikely because the IGM maintains a fairly high neutral fraction at these redshifts. EoR LAEs are thought to be more readily observable if they sit within ionized bubbles, wherein the emitted Lyα is protected by an ionized region large enough for the Lyα photons to scatter out of resonance with the neutral IGM and remain observable. Similar works reporting EoR Lyα detections note potential overdensities near their targets (e.g., Jung et al. 2020; Endsley et al. 2021; Larson et al. 2022), and suggest these overdensities can support larger (and therefore more easily detectable) ionized bubbles. The threshold radius for Lyα observability has been approximated at ~1 physical Mpc (Dijkstra et al. 2014) before resonant scattering is sufficiently diminished as photons are cosmologically redshifted. The exact scale of this size depends on the Lyα

velocity offset from the systemic redshift, which would reduce this threshold to a smaller radius.

Importantly, without constraints for Lyα EW, Lyα escape fraction, and/or velocity offset from systemic redshift, we cannot reliably measure the existence of an ionized bubble in our sample. However, following discussions in other works (e.g., Tilvi et al. 2020; Jung et al. 2022), we search our data for any close pairs or groups indicative of a potential overdensity to explore the possibility of an ionized bubble in such regions as a thought experiment.

We identify one potential overdensity in the WERLS MOSFIRE sample, with two targets at $z = 7.68$ in the COSMOS field: WERLS_786362 at $z = 7.6810$ and WERLS_9030 at $z = 7.6862$. Given their proximity in redshift of $\Delta z = 0.0052$, this pair has a very small line-of-sight separation of 0.2 pMpc, less than half the line-of-sight separations of the $z = 7.7$ galaxy group in EGS77 (0.7 pMpc; Tilvi et al. 2020). However, the two galaxies are more distant in projection at a separation of 9.″6, corresponding to a transverse separation of 2.9 pMpc.

Following the methods in Endsley et al. (2021) and Larson et al. (2022), we estimate the expected ionized bubble radius that would be produced by each galaxy, assuming no Lyα velocity offset because we lack systemic redshifts for these targets (effectively, this serves as an upper limit). From Cen & Haiman (2000) and Endsley et al. (2021), we calculate the ionized bubble radius R produced by each galaxy as

$$R = \left(\frac{3\, \dot{N}_{\rm ion}\, f_{\rm esc}\, t}{4\, \pi\, n_{\rm HI}(z)} \right)^{1/3}. \quad (1)$$

Considering first the denominator, the proper volume density of neutral hydrogen ($n_{\rm HI}(z)$) can be derived from cosmological parameters (see Equations (2) and (3) in Larson et al. 2022). We adopt Planck measurements of the helium mass fraction, Hubble constant, and baryon density (Planck Collaboration 2016, 2020).

Each variable in the numerator represents the ionizing production, output, and transmission from the individual galaxy. The ionizing production is represented by t, the duration of the current star formation episode; for our targets this is unconstrained, so we follow Larson et al. (2022) and take $t = 20$ Myr, noting that a longer episode would increase the bubble's radius. The transmission of ionizing photons is represented by the escape fraction ($f_{\rm esc}$), which is unconstrained for our targets; we allow this parameter to vary from [0–1], and calculate bubble radius as a function of $f_{\rm esc}$. Finally, the ionizing photon output from the galaxy is represented by the intrinsic ionizing emissivity, $\dot{N}_{\rm ion}$.

We calculate $\dot{N}_{\rm ion}$ from the product of the ionizing photons production efficiency ($\xi_{\rm ion}$) and the specific nonionizing UV luminosity ($\rho_{\rm UV}$). Here, we assume $\xi_{\rm ion} = 25.6$ to be consistent with measurements of $\xi_{\rm ion}$ for both local analogs of EoR galaxies (Tang et al. 2021) and bright EoR sources (Stark 2016), as well as model predictions from Finkelstein et al. (2019). Finally, $\rho_{\rm UV}$ can be estimated from the observed brightness of the galaxy (here, its apparent H-band magnitude) and its redshift.

By applying Equation (1) individually to WERLS_786362 and WERLS_9030, we calculate an ionized bubble radius dependent on the escape fraction (see Figure 9). Taking $f_{\rm esc} = 0.2$ as an example, we find $R = 0.34$ pMpc for WERLS_786362 and $R = 0.31$ pMpc for the slighlty fainter WERLS_9030. As a physically implausible upper bound,

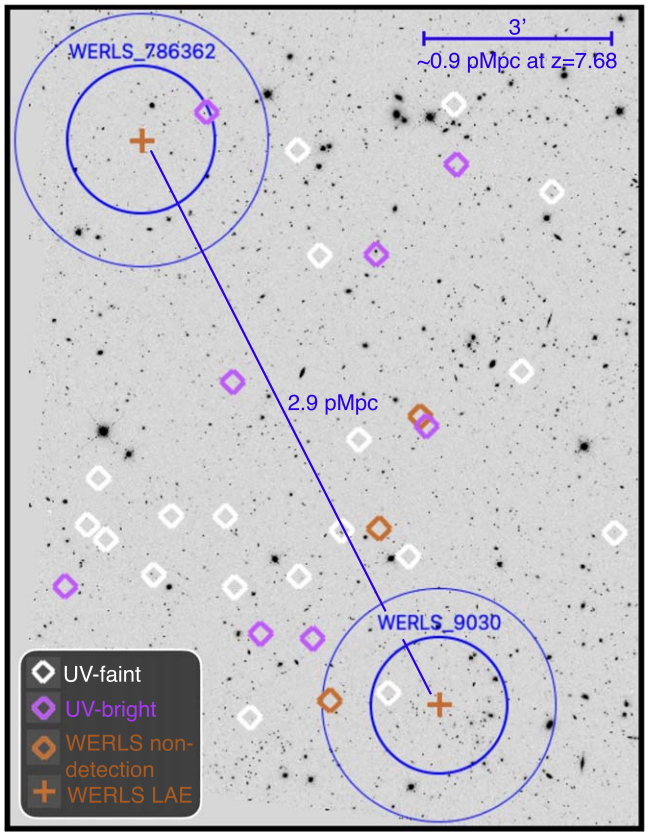

Figure 9. Spatial positions of the two $z = 7.68$ LAEs in our sample (orange plus signs) and the approximate ionized bubbles they would each produce for $f_{\rm esc} = 0.2$ (inner blue circles) and for $f_{\rm esc} = 1.0$ (outer blue circles). The two systems bound a spherical region with radius $R \sim 1.5$ pMpc, a plausible scale for a coherent ionized bubble at this redshift if additional sources contribute to the local ionizing photon budget. The positions of sources at similar photometric redshifts are marked as diamonds, with UV-bright ($M_{\rm UV} \leqslant -20$) sources in purple, UV-faint ($-20 < M_{\rm UV} \leqslant -18$) sources in white, and sources targeted with WERLS MOSFIRE but undetected in Lyα shown in orange. The entire $\sim 9' \times 12'$ region shown here lies within the full COSMOS-Web coverage, with nearly every source also within PRIMER-COSMOS. The figure is projected on the CANDELS HST/F160W image.

allowing all ionizing photons to escape ($f_{\rm esc} = 1.0$) would produce a $R = 0.58$ pMpc bubble for WERLS_786362 and $R = 0.53$ pMpc for WERLS_9030. In the $f_{\rm esc} = 0.2$ case, estimated bubble sizes are about 5 × smaller than the spherical region defined by the observed separation between the galaxies ($R = 1.5$ pMpc); even in the $f_{\rm esc} = 1.0$ case, the sum of the individual bubble radii (1.1 pMpc) is less than the galaxies' separation. Therefore, we determine that the physical scenario wherein their individual ionized bubbles alone can easily overlap and create a common, larger ionized bubble is unlikely. Note that in the case where the intrinsic Lyα emission is much stronger than the observed Lyα line, emission would be observable through a smaller bubble with some significant Lyα loss.

The galaxies' separation is consistent with the expected sizes of ionized regions at $z \sim 7$–8 (Furlanetto et al. 2017; D'Aloisio et al. 2018), as well as observations of large ionized regions (Endsley et al. 2021; Endsley & Stark 2022), and the presence of a large ionized bubble could facilitate the escape of Lyα photons. We consider the possibility that the two LAEs are both embedded in a larger ionized structure of $R \gtrsim 1.5$ pMpc. This scenario is possible if a local overdensity exists in the region, wherein the local ionizing photon budget is supported

by emission from UV-bright galaxies (that may fall outside the WERLS MOSFIRE coverage), and/or fainter EoR galaxies (below the WERLS target criteria). In order to produce a larger ionized bubble encompassing both $z = 7.68$ LAEs in our sample, taking a nominal escape fraction of $f_{\rm esc} = 0.2$, approximately four additional systems of similar ionizing power at similar redshifts would need to be located within a $\sim$23 arcmin^2 area. We search the COSMOS CANDELS catalog for galaxies at $7.58 \leqslant z_{\rm phot} \leqslant 7.78$ within a $\sim 5'$ radius circle bounded by the two WERLS LAEs, and find 10 (30) candidates with $M_{\rm UV} \leqslant -20$ ($-20 < M_{\rm UV} \leqslant -18$). Three of the 10 UV-bright sources were targeted with WERLS and were not detected in Lyα. Figure 9 shows the spatial distribution of the LAEs and potential nearby systems. As noted before, this discussion serves as a thought experiment exploring the possibility of an ionized bubble within our data set; the existence of such a bubble cannot be reliably measured or confirmed without additional spectroscopy for a more complete sample of galaxies within this potential large ionized region. Targeting the remaining candidates—including sources fainter than the WERLS criteria—to search for other nearby LAEs at $z \sim 7.68$ offers an explicit hypothesis that can be tested with future MOSFIRE observations to determine if the $z = 7.68$ LAEs reported here occupy a single, larger ionized bubble.

5.3. WERLS Synergy with JWST

While the aim of the WERLS Keck spectroscopy is to detect Lyα from UV-bright EoR galaxies that likely trace high density peaks, the ultimate goal of the WERLS experiment is to use this census of Lyα emission to then map the ionization state of the Universe and better constrain both the sources and process of reionization. This broader goal relies on planned and upcoming JWST/NIRCam deep imaging. COSMOS-Web, CEERS, and PRIMER will be able to construct detailed maps of the underlying mass in large-scale structure on $(5\,{\rm Mpc})^3$ scales by detecting thousands of EoR galaxies at luminosities $10-30\times$ fainter than our UV-bright WERLS targets. By design, the majority of our targets sit within COSMOS-Web because the survey is large enough to mitigate cosmic variance and to capture reionization on scales larger than its expected patchiness. The smaller but deeper CEERS and PRIMER surveys cover areas comparable to a single ionized bubble in the EoR, but include fainter sources and provide a finer sampling of ionized bubbles; the cosmological context of bubbles found in these deeper programs can then be informed by the larger statistical samples in COSMOS-Web.

This WERLS synergy between JWST imaging and Keck spectroscopy to pinpoint beacons of reionization via Lyα detection and then map the underlying galaxy density can tell us which galaxies are primarily responsible for reionizing the Universe. Upon completion of both the NIRCam surveys and the full Keck WERLS program, we plan to make this measurement through careful cross-correlation of the two maps (in particular using a two-point correlation function). From these maps, we will test the hypothesis that either massive, intrinsically bright galaxies drove reionization in highly clustered regions or that more common low-mass galaxies drive a more homogeneous reionization process.

WERLS synergy with JWST is also powerful from an entirely spectroscopic context. By design, WERLS is a Lyα detection experiment; indeed, given the neutral fraction of the IGM halfway through the EoR, we do not expect to detect Lyα in most of our EoR targets. Given the lack of other emission lines near the target Lyα emission line, there exists some uncertainty in spectroscopic confirmation, for both detections and nondetections. NIRSpec observations can provide, both for LAEs and nonLAEs, unambiguous spectroscopic confirmation via multiple rest-frame optical emission lines.

The five NIRSpec-derived redshifts for both LAEs and nonLAEs in WERLS allows broader exploration of the Lyα-detection experiment goal of WERLS. With MOSFIRE, we obtain deep, high-resolution spectra ($R \sim 3500$) of Lyα from our sources, which serves as a crucial step in the detection experiment. For example, while we detect Lyα in our MOSFIRE observation of WERLS_32350, Jung et al. (2024) did not detect Lyα from WERLS_32350 (referred to in their work as z8_32350) with their medium resolution NIRSpec G140M grating data, which they attribute to the faintness of its Lyα emission, below the detection limit. The case of WERLS_40898—a NIRSpec-confirmed LAE that was undetected in WERLS because of the presence of an atmospheric line at the expected wavelength of the line—demonstrates one challenge of ground-based near-infrared observing and serves as a reminder that care should be taken when interpreting results related to completeness and yield for this survey and others like it; we account for sky line contamination in our LAE yield estimation in Section 5.1. Additionally, we are able to securely confirm two WERLS targets (WERLS_35089 and WERLS_45153) as nonLAEs via their NIRSpec spectra. These cases demonstrate the synergy between the WERLS/Keck observations targeting Lyα with deep, high-resolution near-infrared spectra from the ground, and relatively inexpensive multiline spectroscopic confirmation from JWST/NIRSpec; with these two instruments, the WERLS Lyα detection experiment can be robustly and efficiently conducted.

6. Summary

In this paper, we present the first results from the WERLS program, specifically Keck I/MOSFIRE *Y*-band spectroscopic observations for 114 known, UV-bright EoR candidates in COSMOS, EGS, and UDS. We summarize our results as follows:

1. We spectroscopically identify 11 LAEs from $z \sim 7$–8, with three secure and eight tentative LAEs spanning Lyα-derived spectroscopic redshifts of $7.0925 \leqslant z \leqslant 8.3868$ and absolute UV magnitudes of $-23.14 < M_{\rm UV} < -19.81$.
2. We find an observed LAE yield of $\sim$13%, which is broadly consistent with expectations for a Universe that is half-ionized at $z \sim 7$–8, illustrating the success of WERLS at detecting Lyα in UV-bright EoR galaxies.
3. We identify one potential overdensity in the WERLS MOSFIRE sample, with two targets at $z = 7.68$ in the COSMOS field that are separated by 2.9 pMpc (9.′6). Based on their estimated individual ionized bubble radii, the two galaxies could occupy a common ionized bubble if nearby galaxies within a $\sim$1.5 pMpc volume ($\sim$4 UV-bright galaxies for a nominal $f_{\rm esc} = 0.2$) contribute to the local ionizing photon budget.

The first year of WERLS has demonstrated its efficacy at detecting LAEs near the midpoint of the EoR. Combined with large-scale mass density maps of the field derived from deep JWST/NIRCam imaging, future synergistic Keck+JWST efforts provide a powerful tool for pinpointing beacons of

reionization and mapping the ionization state of the Universe, enabling robust tests regarding the primary drivers and the timeline of reionization.

Acknowledgments

The authors wish to recognize and acknowledge the very significant cultural role and reverence that the summit of Maunakea has always had within the indigenous Hawaiian community. We are most fortunate to have the opportunity to conduct observations from this mountain.

O.R.C, C.M.C., and others at UT Austin acknowledge that they work at an institution that sits on indigenous land. The Tonkawa lived in central Texas, and the Comanche and Apache moved through this area. We pay our respects to all the American Indian and Indigenous Peoples and communities who have been or have become a part of these lands and territories in Texas. We are grateful to be able to live, work, collaborate, and learn on this piece of Turtle Island.

We would like to thank the `PypeIt` team for help in the reduction and customization work for `PypeIt`/MOSFIRE, in particular Debora Pelliccia.

This work was supported by PID40/2022A_N078 (PIs C. Casey & J. Kartaltepe). Data presented herein were obtained at the W. M. Keck Observatory from telescope time allocated to the National Aeronautics and Space Administration through the agency's scientific partnership with the California Institute of Technology and the University of California. The Observatory was made possible by the generous financial support of the W. M. Keck Foundation.

This material is based on work supported by the National Science Foundation Graduate Research Fellowship under grant number DGE 2137420.

This work is partly based on observations made with the NASA/ESA/CSA *JWST*. The data were obtained from the Mikulski Archive for Space Telescopes at the Space Telescope Science Institute, which is operated by the Association of Universities for Research in Astronomy, Inc., under NASA contract NAS 5-03127 for JWST. These observations are associated with programs JWST-ERS-01345 and JWST-GO-01837.

C.M.C. thanks the National Science Foundation for support through grants AST-1814034 and AST-2009577, as well as the University of Texas at Austin College of Natural Sciences for support; C.M.C. also acknowledges support from the Research Corporation for Science Advancement from a 2019 Cottrell Scholar Award sponsored by IF/THEN, an initiative of Lyda Hill Philanthropies.

J.S.K. thanks the National Science Foundation for support through grant AST-2009572. J.S.K. and B.N.V. thank NASA/California Institute of Technology-JPL for support through grant 1668074. A.B. thanks the Emerson Summer Undergraduate Research Fellowship through the College of Science at the Rochester Institute of Technology.

The authors would like to thank our Keck Observatory Support Astronomers, Jim Lyke and Chien-Hsiu Lee, for their assistance during our observing runs. Special thanks to all of our Observing Assistants for their work driving the telescope during our observations: Matthew (Matt) Wahl, Marita (Rita) Morris, Tony Ridenour, Carolyn Jordan, and John Pelletier.

Facility: Keck:I (MOSFIRE).

Software: `astropy` (Astropy Collaboration et al. 2013, 2018, 2022), `numpy` (Harris et al. 2020), EAZY (Brammer et al. 2008), LEPHARE (Arnouts & Ilbert 2011), `Jupyter` (Kluyver et al. 2016), `matplotlib` (Caswell et al. 2023), `scipy` (Virtanen et al. 2020), SOURCEEXTRACTOR (Bertin & Arnouts 1996), STScI JWST Calibration Pipeline (jwst-pipeline.readthedocs.io; Rigby et al. 2023), MAGMA (www2.keck.hawaii.edu/inst/mosfire/magma.html), `PypeIt` (Prochaska et al. 2020), MOSFIREDRP (keck-datareductionpipelines.github.io/MosfireDRP), `Bagpipes` (Carnall et al. 2018), `photutils` (Bradley et al. 2023), `pypher` (Boucaud et al. 2016), `grizli` (Brammer 2023).

Data Availability

The target list and spectroscopic results presented herein are available in machine-readable format; see Appendix and Tables 4 and 5. Reduced MOSFIRE spectra will be provided upon request.

Appendix
Spectroscopic Catalog

Here, we provide the full target list, any emission line detections, and any new spectroscopic redshift measurements for the Keck/MOSFIRE observations presented in this paper. Spectroscopic confirmation of EoR LAEs (our primary targets) is discussed in Section 4.2 of the main text; here, we also include the majority of our spectroscopic confirmations, which were lower-redshift filler targets.

Filler targets are selected at specific redshifts with emission lines accessible with MOSFIRE *Y*-band; Hα-emitters at $0.5 < z < 0.7$, [O II]-emitters at $1.6 < z < 2.0$, and CIII]-emitters at $4.1 < z < 4.9$. Stars (for alignment and for flux calibration) were also placed on each mask; these are taken from Gaia DR3 and registered to the same reference astrometry as our source catalogs. Any serendipitously observed sources (with naming convention SERENDIP-X with X being an arbitrary number) are also included in the catalog. Positions of the serendipitous detections are carefully reconstructed using deep imaging and relative offset of other sources on the mask, accurate to $\sim 0\farcs5$. Table 4 shows the first few lines of the data table with the source ID, slit mask, and position of all observed targets, which includes primary targets, filler targets, stars, and serendipitous sources. The full target list is provided in machine-readable form online.

A total of 330 targets were observed, with 114 primary targets, 15 stars, 35 serendipitous sources, and 166 filler targets. The spectroscopic yield for filler targets is $\sim$34%, including all

Table 4
WERLS/MOSFIRE 2022A Target List

ID	Mask	R.A.	Decl.
M_WP551495	wmmc01	150.19379	2.17021
B_WP450980	wmmc01	150.18992	2.16204
star_75	wmmc01	150.19183	2.18124
L_WP693466	wmmc01	150.18879	2.18037
SERENDIP-1	wmmc01	150.18644	2.18126
c2020_pz_0.664_22.8_826089	wmmc01	150.18738	2.19157
L_WP930991	wmmc01	150.18792	2.20266
c2020_pz_1.65_22.6_640174	wmmc01	150.17921	2.17518
c2020_pz_4.25_27.1_702146	wmmc01	150.17733	2.18104

Notes. Table 4 is published in its entirety in machine-readable format. A portion is shown here for guidance regarding its form and content.

(This table is available in its entirety in machine-readable form.)

Table 5
WERLS/MOSFIRE 2022A Spectroscopic Catalog

ID	Redshift	λ_{obs} Å	Line Species	Confidence Class[a]	Notes
M_WP551495	…	…	…	0	
B_WP450980	7.0925	9837	Lyα	2	Tentative_in_paper
star_75	…	…	…	−1	
L_WP693466	…	…	…	0	
SERENDIP-1	…	10945	…	0	
c2020_pz_0.664_22.8_826089	0.667	10936	Hα	4	
L_WP930991	…	…	…	0	
c2020_pz_1.65_22.6_640174	1.641	9848	[O II]	4	
c2020_pz_4.25_27.1_702146	…	…	…	0	

Notes. Table 5 is published in its entirety in machine-readable format. A portion is shown here for guidance regarding its form and content.
[a] Quality flag indicating confidence class of spectroscopic confirmation, where 0=no redshift measurement attempted, 1 = an insecure redshift, 2 = a likely redshift about which there is some doubt, 3 = a very secure redshift, 4 = a very secure redshift with an exhibition-quality spectrum, 9 = a securely detected single line with prior information that enables redshift identification, and −1 = continuum detection without line detection.

(This table is available in its entirety in machine-readable form.)

56 spectroscopic redshift identifications, whether tentative (39/56) or secure (17/56). We note observed line wavelengths for serendipitous sources. However, in all cases except when multiple lines enabled line species identification (e.g., Magee et al. 2023), we do not list line or redshift identifications given their lack of photometric redshift priors in the WERLS target catalog.

Importantly, quality flags indicating confidence class of spectroscopic confirmation are also included in the table. We follow the convention in the zCOSMOS catalog as described in Lilly et al. (2009), wherein 0 = no redshift measurement attempted, 1 = an insecure redshift, 2 = a likely redshift about which there is some doubt, 3 = a very secure redshift, 4 = a very secure redshift with an exhibition-quality spectrum, and 9 = a securely detected single line with prior information that enables redshift identification. We add to this convention scheme the confidence class −1 to indicate continuum detection without line detection, which was only relevant for the stars and for a handful of serendipitous sources. All primary targets in the paper are classified with confidence class of 2 for tentative LAEs or 9 for secure LAEs; these are also indicated in the notes column by "tentative_in_paper" or "secure_in_paper," respectively. Candidate LAEs that were included in the early vetting process (as described in Section 3.2) but ultimately excluded from this paper are classified with quality flags of 1, and noted by "early_vetting" in the notes. For fillers, only sources with confidence classes of 3 or 4 should be considered secure redshifts because these are the only multiline detections. Measurements for all other filler targets should be considered tentative. The first few lines of the spectroscopic data table are shown in Table 5, with the full table provided in machine-readable form online.

ORCID iDs

Olivia R. Cooper https://orcid.org/0000-0003-3881-1397
Caitlin M. Casey https://orcid.org/0000-0002-0930-6466
Hollis B. Akins https://orcid.org/0000-0003-3596-8794
Stephanie M. Urbano Stawinski https://orcid.org/0000-0001-8169-7249
Jeyhan S. Kartaltepe https://orcid.org/0000-0001-9187-3605
Steven L. Finkelstein https://orcid.org/0000-0001-8519-1130
Rebecca L. Larson https://orcid.org/0000-0003-2366-8858
Intae Jung https://orcid.org/0000-0003-1187-4240
Jaclyn B. Champagne https://orcid.org/0000-0002-6184-9097
Óscar A. Chávez Ortiz https://orcid.org/0000-0003-2332-5505
Sadie Coffin https://orcid.org/0000-0003-3038-8045
M. C. Cooper https://orcid.org/0000-0003-1371-6019
Nicole Drakos https://orcid.org/0000-0003-4761-2197
Andreas L. Faisst https://orcid.org/0000-0002-9382-9832
Maximilien Franco https://orcid.org/0000-0002-3560-8599
Seiji Fujimoto https://orcid.org/0000-0001-7201-5066
Steven Gillman https://orcid.org/0000-0001-9885-4589
Ghassem Gozaliasl https://orcid.org/0000-0002-0236-919X
Santosh Harish https://orcid.org/0000-0003-0129-2079
Taylor A. Hutchison https://orcid.org/0000-0001-6251-4988
Anton M. Koekemoer https://orcid.org/0000-0002-6610-2048
Vasily Kokorev https://orcid.org/0000-0002-5588-9156
Jitrapon Lertprasertpong https://orcid.org/0000-0002-3535-4066
Daizhong Liu https://orcid.org/0000-0001-9773-7479
Arianna S. Long https://orcid.org/0000-0002-7530-8857
Casey Papovich https://orcid.org/0000-0001-7503-8482
R. Michael Rich https://orcid.org/0000-0003-0427-8387
Brant E. Robertson https://orcid.org/0000-0002-4271-0364
Margherita Talia https://orcid.org/0000-0003-4352-2063
Brittany N. Vanderhoof https://orcid.org/0000-0002-8163-0172
John R. Weaver https://orcid.org/0000-0003-1614-196XR
Katherine E. Whitaker https://orcid.org/0000-0001-7160-3632
Jorge A. Zavala https://orcid.org/0000-0002-7051-1100

References

Arnouts, S., Cristiani, S., Moscardini, L., et al. 1999, MNRAS, 310, 540
Arnouts, S., & Ilbert, O., 2011 LePHARE: Photometric Analysis for Redshift Estimate, Astrophysics Source Code Library, ascl:1108.009
Arons, J., & McCray, R. 1970, ApL, 5, 123
Arrabal Haro, P., Dickinson, M., Finkelstein, S. L., et al. 2023, ApJ, 951, L22
Ashby, M. L. N., Willner, S. P., Fazio, G. G., et al. 2015, ApJS, 218, 33
Astropy Collaboration, Price-Whelan, A. M., Lim, P. L., et al. 2022, ApJ, 935, 167
Astropy Collaboration, Price-Whelan, A. M., Sipőcz, B. M., et al. 2018, AJ, 156, 123
Astropy Collaboration, Robitaille, T. P., Tollerud, E. J., et al. 2013, A&A, 558, A33
Becker, G. D., Bolton, J. S., Madau, P., et al. 2015, MNRAS, 447, 3402
Bertin, E., & Arnouts, S. 1996, A&AS, 117, 393

Böker, T., Beck, T. L., Birkmann, S. M., et al. 2023, PASP, 135, 038001
Bolan, P., Lemaux, B. C., Mason, C., et al. 2022, MNRAS, 517, 3263
Bosman, S. E. I., Davies, F. B., Becker, G. D., et al. 2022, MNRAS, 514, 55
Boucaud, A., Bocchio, M., Abergel, A., et al. 2016, A&A, 596, A63
Bouwens, R. J., Smit, R., Schouws, S., et al. 2022, ApJ, 931, 160
Bradley, L., Sipőcz, B., Robitaille, T., et al. 2023, Astropy/Photutils: 1.9.0, v1.9.0, Zenodo, doi:10.5281/zenodo.8248020
Brammer, G. 2023, grizli, v1.9.11, Zenodo, doi:10.5281/zenodo.8370018
Brammer, G. B., van Dokkum, P. G., & Coppi, P. 2008, ApJ, 686, 1503
Bremer, J., & Dayal, P. 2023, MNRAS, 524, 118
Bunker, A. J., Saxena, A., Cameron, A. J., et al. 2023, A&A, 677, A88
Bunker, A. J., Wilkins, S., Ellis, R. S., et al. 2010, MNRAS, 409, 855
Burgasser, A. J., Gerasimov, R., Bezanson, R., et al. 2024, ApJ, 962, 177
Bushouse, H., Eisenhamer, J., Dencheva, N., et al. 2022, JWST Calibration Pipeline, v1.8.2, Zenodo, doi:10.5281/zenodo.7325378
Byler, N., Dalcanton, J. J., Conroy, C., & Johnson, B. D. 2017, ApJ, 840, 44
Calzetti, D. 2001, PASP, 113, 1449
Cameron, A. J., Saxena, A., Bunker, A. J., et al. 2023, A&A, 677, A115
Carnall, A. C., McLure, R. J., Dunlop, J. S., & Davé, R. 2018, MNRAS, 480, 4379
Casey, C. M., Kartaltepe, J. S., Drakos, N. E., et al. 2023, ApJ, 954, 31
Castellano, M., Dayal, P., Pentericci, L., et al. 2016, ApJ, 818, L3
Castelli, F., & Kurucz, R. L. 2003, in IAU Symp. 210, Modelling of Stellar Atmospheres, Poster Contributions, ed. N. Piskunov, W. W. Weiss, & D. F. Gray (San Francisco, CA: ASP), A20
Caswell, T. A., de Andrade, E. S., Lee, A., et al., 2023 Matplotlib/Matplotlib: REL: v3.7.2, Zenodo, doi:10.5281/zenodo.8118151
Cen, R., & Haiman, Z. 2000, ApJ, 542, L75
Chabrier, G. 2003, PASP, 115, 763
Conroy, C., White, M., & Gunn, J. E. 2010, ApJ, 708, 58
Curtis-Lake, E., Carniani, S., Cameron, A., et al. 2023, NatAs, 7, 622
D'Aloisio, A., McQuinn, M., Davies, F. B., & Furlanetto, S. R. 2018, MNRAS, 473, 560
Dijkstra, M., Wyithe, S., Haiman, Z., Mesinger, A., & Pentericci, L. 2014, MNRAS, 440, 3309
Dunlop, J. S., Abraham, R. G., Ashby, M. L. N., et al. 2021, PRIMER: Public Release IMaging for Extragalactic Research, JWST Proposal. Cycle 1, ID. #1837
Endsley, R., & Stark, D. P. 2022, MNRAS, 511, 6042
Endsley, R., Stark, D. P., Charlot, S., et al. 2021, MNRAS, 502, 6044
Euclid Collaboration, Moneti, A., McCracken, H. J., et al. 2022, A&A, 658, A126
Faber, S. 2011, The Cosmic Assembly Near-IR Deep Extragalactic Legacy Survey ("CANDELS"), STScI/MAST doi:10.17909/T94S3X
Faisst, A. L. 2016, ApJ, 829, 99
Faisst, A. L., Capak, P., Carollo, C. M., Scarlata, C., & Scoville, N. 2014, ApJ, 788, 87
Ferland, G. J., Chatzikos, M., Guzmán, F., et al. 2017, RMxAA, 53, 385
Finkelstein, S., Bagley, M., & Yang, G. 2023, Data from The Cosmic Evolution Early Release Science Survey (CEERS), STScI/MAST doi:10.17909/Z7P0-8481
Finkelstein, S. L. 2016, PASA, 33, e037
Finkelstein, S. L., Bagley, M., Song, M., et al. 2022, ApJ, 928, 52
Finkelstein, S. L., D'Aloisio, A., Paardekooper, J.-P., et al. 2019, ApJ, 879, 36
Finkelstein, S. L., Papovich, C., Dickinson, M., et al. 2013, Natur, 502, 524
Finkelstein, S. L., Papovich, C., Giavalisco, M., et al. 2010, ApJ, 719, 1250
Finkelstein, S. L., Papovich, C., Ryan, R. E., et al. 2012, ApJ, 758, 93
Flury, S. R., Jaskot, A. E., Ferguson, H. C., et al. 2022, ApJS, 260, 1
Fujimoto, S., Arrabal Haro, P., Dickinson, M., et al. 2023, ApJ, 949, L25
Furlanetto, S. R., Mirocha, J., Mebane, R. H., & Sun, G. 2017, MNRAS, 472, 1576
Gaia Collaboration, Vallenari, A., Brown, A. G. A., et al. 2023, A&A, 674, A1
Grogin, N. A., Kocevski, D. D., Faber, S. M., et al. 2011, ApJS, 197, 35
Hainline, K. N., Helton, J. M., Johnson, B. D., et al. 2024, ApJ, 964, 66
Harish, S., Wold, I. G. B., Malhotra, S., et al. 2022, ApJ, 934, 167
Harris, C. R., Millman, K. J., van der Walt, S. J., et al. 2020, Natur, 585, 357
Hashimoto, T., Laporte, N., Mawatari, K., et al. 2018, Natur, 557, 392
Heintz, K. E., Brammer, G. B., Giménez-Arteaga, C., et al. 2023, NatAs, 7, 1517
Hoag, A., Bradač, M., & Brammer, G. 2018, ApJ, 854, 39
Hoag, A., Bradač, M., Huang, K., et al. 2019, ApJ, 878, 12
Hoag, A., Bradač, M., Trenti, M., et al. 2017, NatAs, 1, 0091
Horne, K. 1986, PASP, 98, 609
Hu, W., Wang, J., Infante, L., et al. 2021, NatAs, 5, 485
Hu, W., Wang, J., Zheng, Z.-Y., et al. 2019, ApJ, 886, 90
Hutchison, T. A., Walawender, J., & Kwok, S. H. 2020, Proc. SPIE, 11447, 114476A
Ilbert, O., Arnouts, S., McCracken, H. J., et al. 2006, A&A, 457, 841
Inoue, A. K., Tamura, Y., Matsuo, H., et al. 2016, Sci, 352, 1559
Izotov, Y. I., Schaerer, D., Thuan, T. X., et al. 2016, MNRAS, 461, 3683
Izotov, Y. I., Schaerer, D., Worseck, G., et al. 2018, MNRAS, 474, 4514
Jiang, H., Wang, X., Cheng, C., et al. 2023, arXiv:2312.04151
Jones, G. C., Bunker, A. J., Saxena, A., et al. 2024, A&A, 683, A238
Jung, I., Finkelstein, S. L., Arrabal Haro, P., et al. 2024, ApJ, 967, 73
Jung, I., Finkelstein, S. L., Dickinson, M., et al. 2019, ApJ, 877, 146
Jung, I., Finkelstein, S. L., Dickinson, M., et al. 2020, ApJ, 904, 144
Jung, I., Finkelstein, S. L., Larson, R. L., et al. 2022, arXiv.2212.09850
Kakiichi, K., Dijkstra, M., Ciardi, B., & Graziani, L. 2016, MNRAS, 463, 4019
Kannan, R., Garaldi, E., Smith, A., et al. 2022, MNRAS, 511, 4005
Kluyver, T., Ragan-Kelley, B., Pérez, F., et al. 2016, in Positioning and Power in Academic Publishing: Players, Agents and Agendas, ed. F. Loizides & B. Schmidt (Amsterdam: IOS Press) 87
Koekemoer, A. M., Faber, S. M., Ferguson, H. C., et al. 2011, ApJS, 197, 36
Kriek, M., Shapley, A. E., Reddy, N. A., et al. 2015, ApJS, 218, 15
Laigle, C., McCracken, H. J., Ilbert, O., et al. 2016, ApJS, 224, 24
Langeroodi, D., Hjorth, J., & Zhang, Z. 2023, ApJL, 957, L27
Larson, R. L., Finkelstein, S. L., Hutchison, T. A., et al. 2022, ApJ, 930, 104
Leja, J., Carnall, A. C., Johnson, B. D., Conroy, C., & Speagle, J. S. 2019, ApJ, 876, 3
Lilly, S. J., Le Brun, V., Maier, C., et al. 2009, ApJS, 184, 218
Magee, J., Casey, C. M., Cooper, O. R., et al. 2023, RNAAS, 7, 110
Marley, M. S., Saumon, D., Visscher, C., et al. 2021, ApJ, 920, 85
Marques-Chaves, R., Schaerer, D., Álvarez-Márquez, J., et al. 2021, MNRAS, 507, 524
Mason, C. A., Fontana, A., Treu, T., et al. 2019, MNRAS, 485, 3947
Mason, C. A., Trenti, M., & Treu, T. 2015, ApJ, 813, 21
Massey, F. J., Jr. 1951, J. Am. Stat. Assoc., 46, 68
McCracken, H. J., Milvang-Jensen, B., Dunlop, J., et al. 2012, A&A, 544, A156
McElwain, M. W., Feinberg, L. D., Perrin, M. D., et al. 2023, PASP, 135, 058001
McLean, I. S., Steidel, C. C., Epps, H. W., et al. 2012, Proc. SPIE, 8446, 84460J
McLure, R. J., Dunlop, J. S., Cirasuolo, M., et al. 2010, MNRAS, 403, 960
Menzel, M., Davis, M., Parrish, K., et al. 2023, PASP, 135, 058002
Naidu, R. P., Tacchella, S., Mason, C. A., et al. 2020, ApJ, 892, 109
Nakane, M., Ouchi, M., Nakajima, K., et al. 2024, ApJ, 967, 28
Oesch, P. A., Bouwens, R. J., Illingworth, G. D., et al. 2012, ApJ, 759, 135
Oesch, P. A., Brammer, G., Naidu, R. P., et al. 2023, MNRAS, 525, 2864
Oesch, P. A., van Dokkum, P. G., Illingworth, G. D., et al. 2015, ApJ, 804, L30
Oke, J. B., Cohen, J. G., Carr, M., et al. 1995, PASP, 107, 375
Oke, J. B., & Gunn, J. E. 1983, ApJ, 266, 713
Ono, Y., Ouchi, M., Mobasher, B., et al. 2012, ApJ, 744, 83
Ouchi, M., Ono, Y., & Shibuya, T. 2020, ARA&A, 58, 617
Paardekooper, J.-P., Khochfar, S., & Dalla Vecchia, C. 2015, MNRAS, 451, 2544
Pentericci, L., Vanzella, E., Castellano, M., et al. 2018, A&A, 619, A147
Planck Collaboration, Ade, P. A. R., Aghanim, N., et al. 2016, A&A, 594, A13
Planck Collaboration, Aghanim, N., Akrami, Y., et al. 2020, A&A, 641, A6
Prochaska, J. X., Hennawi, J., Cooke, R., et al. 2020, pypeit/PypeIt: Release 1.0.0, v1.0.0, Zenodo, doi:10.5281/zenodo.3743493
Rieke, M. J., Kelly, D. M., Misselt, K., et al. 2023, PASP, 135, 028001
Rigby, J., Perrin, M., McElwain, M., et al. 2023, PASP, 135, 048001
Roberts-Borsani, G., Treu, T., Mason, C., et al. 2023, ApJ, 948, 54
Roberts-Borsani, G. W., Bouwens, R. J., Oesch, P. A., et al. 2016, ApJ, 823, 143
Robertson, B. E., Furlanetto, S. R., Schneider, E., et al. 2013, ApJ, 768, 71
Rockosi, C., Stover, R., Kibrick, R., et al. 2010, Proc. SPIE, 7735, 77350R
Saha, K., Tandon, S. N., Simmonds, C., et al. 2020, NatAs, 4, 1185
Sanders, R. L., Shapley, A. E., Topping, M. W., Reddy, N. A., & Brammer, G. B. 2024, ApJ, 962, 24
Saxena, A., Bunker, A. J., Jones, G. C., et al. 2024, A&A, 684, A84
Saxena, A., Robertson, B. E., Bunker, A. J., et al. 2023a, A&A, 678, A68
Schouws, S., Stefanon, M., Bouwens, R., et al. 2022, ApJ, 928, 31
Shibuya, T., Kashikawa, N., Ota, K., et al. 2012, ApJ, 752, 114
Smit, R., Bouwens, R. J., Carniani, S., et al. 2018, Natur, 553, 178
Smit, R., Bouwens, R. J., Franx, M., et al. 2015, ApJ, 801, 122
Song, M., Finkelstein, S. L., Livermore, R. C., et al. 2016, ApJ, 826, 113
Stark, D. P. 2016, ARA&A, 54, 761
Stark, D. P., Ellis, R. S., Charlot, S., et al. 2017, MNRAS, 464, 469
Tacchella, S., Finkelstein, S. L., Bagley, M., et al. 2022, ApJ, 927, 170

Tang, M., Stark, D. P., Chen, Z., et al. 2023, MNRAS, 526, 1657
Tang, M., Stark, D. P., Chevallard, J., et al. 2021, MNRAS, 503, 4105
Tilvi, V., Malhotra, S., Rhoads, J. E., et al. 2020, ApJ, 891, L10
Treu, T., Schmidt, K. B., Trenti, M., Bradley, L. D., & Stiavelli, M. 2013, ApJ, 775, L29
Virtanen, P., Gommers, R., Oliphant, T. E., et al. 2020, NatMe, 17, 261
Weaver, J., Toft, S., Davidzon, I., Capak, P., & McCracken, H. 2019, in The Art of Measuring Galaxy Physical Properties, 9
Weaver, J. R., Kauffmann, O. B., Ilbert, O., et al. 2022, ApJS, 258, 11
Whitler, L., Stark, D. P., Endsley, R., et al. 2024, MNRAS, 529, 855
Witstok, J., Smit, R., Saxena, A., et al. 2024, A&A, 682, A40
Wold, I. G. B., Malhotra, S., Rhoads, J., et al. 2022, ApJ, 927, 36
Yan, H., Finkelstein, S. L., Huang, K.-H., et al. 2012, ApJ, 761, 177
Zheng, Z., Cen, R., Weinberg, D., Trac, H., & Miralda-Escudé, J. 2011, ApJ, 739, 62
Zitrin, A., Ellis, R. S., Belli, S., & Stark, D. P. 2015, ApJ, 805, L7